Hydraulic fracturing and active coarsening position the lumen of the mouse blastocyst

Julien G Dumortier, Mathieu Le Verge-Serandour, Anna Francesca Tortorelli, Annette Mielke, Ludmilla de Plater, Hervé Turlier, Jean-Léon Maître

HAL Id: hal-02315507

https://hal.sorbonne-universite.fr/hal-02315507v1

Submitted on 14 Oct 2019

Hydraulic fracturing and active coarsening position the lumen of the mouse blastocyst

Julien G. Dumortier[1], Mathieu Le Verge-Serandour[2], Anna-Francesca Tortorelli[1], Annette Mielke[2], Ludmilla de Plater[1], Hervé Turlier[2*] and Jean-Léon Maître[1*]

[1] Institut Curie, PSL Research University, Sorbonne Université, CNRS UMR3215, INSERM U934, Paris, France

[2] Center for Interdisciplinary Research in Biology, Collège de France, PSL Research University, CNRS UMR7241, INSERM U1050, 75005 Paris, France

* Corresponding authors: herve.turlier@college-de-france.fr and jean-leon.maitre@curie.fr
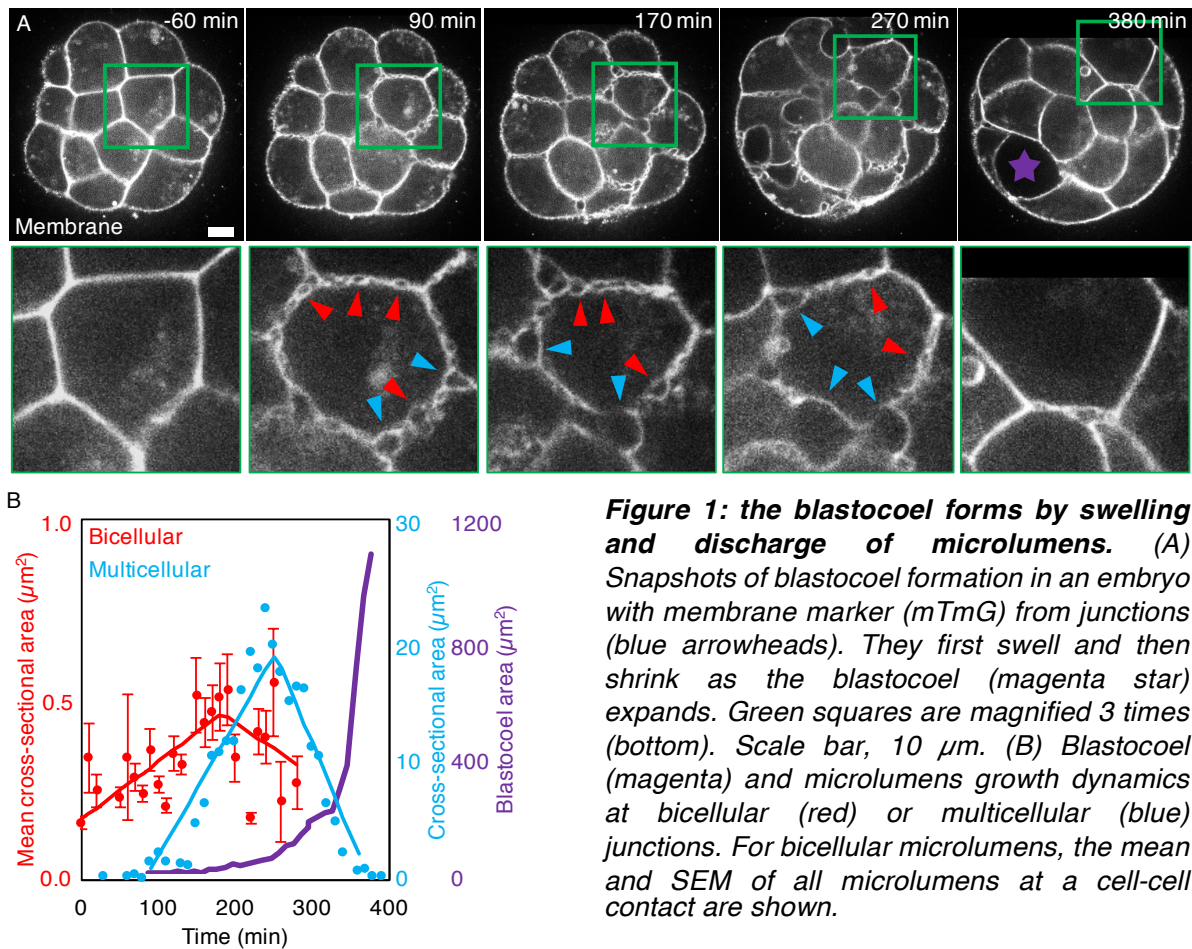
Abstract

During mouse preimplantation development, the formation of the blastocoel, a fluid-filled lumen, breaks the radial symmetry of the blastocyst. What controls the formation and positioning of this basolateral lumen remains obscure. We find that accumulation of pressurized fluid fractures cell-cell contacts into hundreds of micron-size lumens. Microlumens eventually discharge their volumes into a single dominant lumen, which we model as a process akin to Ostwald ripening, underlying the coarsening of foams. Using chimeric mutant embryos, we tune the hydraulic fracturing of cell-cell contacts and steer the coarsening of microlumens, allowing us to successfully manipulate the final position of the lumen. We conclude that hydraulic fracturing of cell-cell contacts followed by contractility-directed coarsening of microlumens sets the first axis of symmetry of the mouse embryo.

Main text

During preimplantation development, the mammalian embryo forms the blastocyst, which consists of a squamous epithelium, the trophectoderm (TE), enveloping the inner cells mass (ICM) and a fluid-filled lumen, the blastocoel (*1-3*). This lumen forms invariably at the interface between ICM and TE cells and segregates the ICM toward one side of the embryo, hence breaking its radial symmetry. This defines the first symmetry axis in the embryo, which guides the position of the main axes of the mammalian body (*4*). External constraints, such as the one provided by the zona pellucida, are thought to guide the orientation of this axis (*5*). However, little is known of the mechanisms that are intrinsic to the embryo. Lumen formation and positioning has been studied in the context of apical lumens (*6*) such as the ones formed in vitro (*7, 8*), or in vivo within the epiblast upon implantation of the blastocyst (*9*). Apicobasal polarity allows building an osmotic gradient that draws water from the outside medium into the apical compartment sealed by tight junctions (*3, 6*). Importantly, the apical membrane is depleted of adhesion molecules and can contain proteins that act as a contact repellent (*10*). This makes the apical membrane weakly adhesive and a favorable interface for the collection of fluid between cells. However, blastocysts are akin to "inverted cysts" (*11, 12*) and form their lumen on the basolateral side of cells, where adhesion molecules concentrate (Fig. S1), making this interface mechanically less favorable for fluid to accumulate from the outside medium (Fig. S2) (*1-3, 13*). Therefore, it is unclear how the blastocoel forms within an adhesive interface and acquires its position between TE and ICM cells.

One possibility would be to separate one or few neighboring TE-ICM contacts and expand the blastocoel from this initial gap (*14*). Alternatively, multiple intercellular gaps could appear between cells, as can be observed between TE cells in electron micrographs of blastocysts from mice (*15*) and non-human primates (*16, 17*), which would merge into a single lumen via unknown mechanisms (*3*). To investigate this, we used mouse embryos expressing a membrane marker (*18*) to perform high-resolution imaging at the onset of lumen formation, when blastomeres have completed their fifth cleavage (Movie 1). We observed hundreds of micron-size lumens (microlumens), forming simultaneously throughout the embryo between cell-cell contacts and at multicellular interfaces (Fig. 1A). Notably, this includes contacts between ICM cells where the blastocoel never forms. The size of microlumens evolves rather synchronously throughout the embryo, showing an initial phase of growth followed by a shrinking period (Fig. S3-5). While eventually most microlumens shrink, one continues expanding and becomes the blastocoel (Fig. 1B). From image and data analysis, we characterized two types of microlumens, at either bicellular or multicellular interfaces, and determined stereotypic parameters describing their evolution: for all microlumens but the blastocoel, we identified a swelling phase followed by a discharge phase (Fig. 1B, Fig. S3, Movie 1). After 87 ± 10 min of steady growth, microlumens between two contacting cells shrink within 68 ± 8 min (Mean ± SEM of 35 contacts from 7 embryos). Compared to bicellular microlumens, multicellular microlumens grow 10 times larger over a similar duration (swelling for 75 ± 21 min and discharge for 65 ± 21 min, Mean ± SEM from 21 multicellular junctions from 7 embryos), as a result of higher swelling and discharge rates (Fig. S3). Interestingly, the phenomenon is rather synchronous with bicellular

2

Figure 1: the blastocoel forms by swelling and discharge of microlumens. *(A) Snapshots of blastocoel formation in an embryo with membrane marker (mTmG) from junctions (blue arrowheads). They first swell and then shrink as the blastocoel (magenta star) expands. Green squares are magnified 3 times (bottom). Scale bar, 10 µm. (B) Blastocoel (magenta) and microlumens growth dynamics at bicellular (red) or multicellular (blue) junctions. For bicellular microlumens, the mean and SEM of all microlumens at a cell-cell contact are shown.*

microlumens appearing within 24 ± 4 min from one another and peaking 25 ± 12 min earlier than multicellular microlumens (Fig. S4-5). From these observations and analysis, we conclude that the formation of the blastocoel does not result from localized separation of contacts between TE and ICM cells specifically. Instead, transient ruptures of cell-cell contacts result in the formation of myriad lumens throughout the embryo that subsequently disappear, leaving only one remaining.

To understand what controls the initiation of the blastocoel, we first investigated how microlumens form at cell-cell contacts. Contacts are enriched in Cdh1, the main cell-cell adhesion molecule of the blastocyst (*19*), which provides them mechanical stability. To visualize the localization of Cdh1 during lumen formation, we generated a transgenic mouse line expressing Cdh1-GFP under its endogenous promoter (*20*) in addition to a membrane marker (*18*). When microlumens form, Cdh1-GFP localization is reorganized, seemingly accumulating at the edges of microlumens (Fig. 2A, Movie 2). This makes the distribution of Cdh1-GFP more heterogeneous (Fig. 2B). The reorganization of Cdh1 could directly result from the accumulation of fluid detaching cell-cell contacts. Such hydraulic fracturing of cell-cell contacts has been described in vitro when fluid, pressurized at a few hundreds of pascals, is flushed through the basolateral side of mature epithelial monolayers (*21*).

Hydraulic fracturing requires to build hydrostatic pressure between cells, first within microlumens and, eventually in the blastocoel. To evaluate the pressure in the blastocoel, we used micropipette aspiration, which allows measuring non-invasively the surface tension and hydrostatic pressure of liquid droplet-like objects (*22*). We
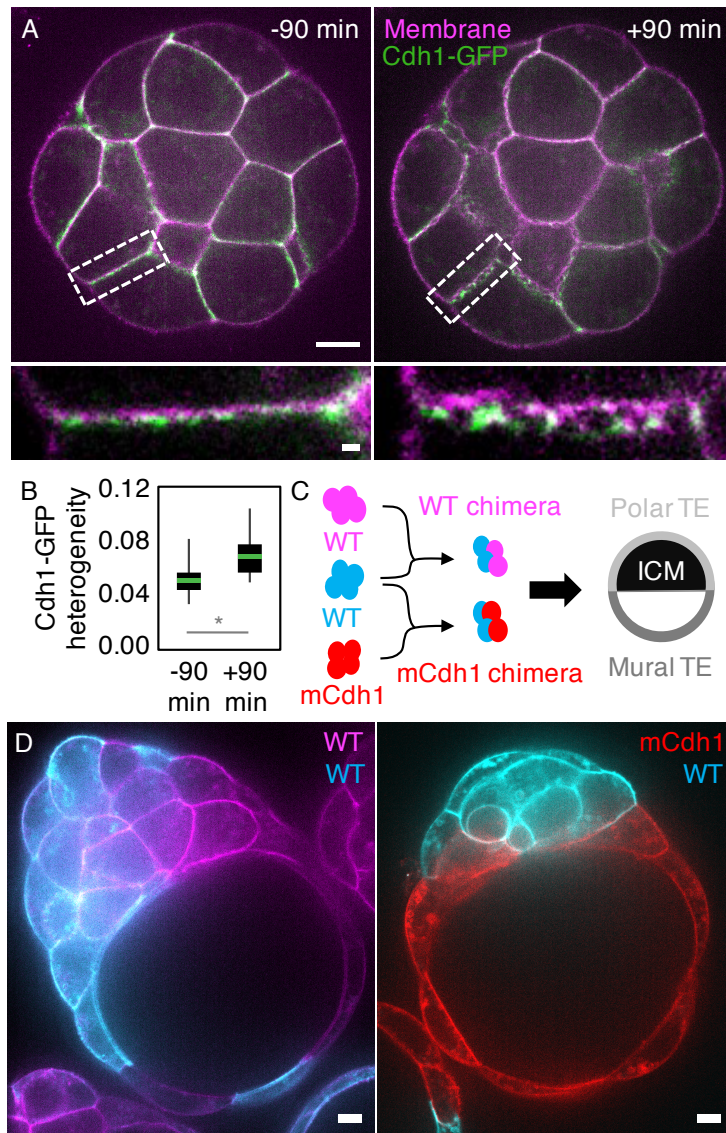
3

Figure 2: hydraulic fracturing can be directed by cell adhesion. *(A) Cdh1-GFP (green) and membrane (magenta) reorganize during microlumen formation. Top shows snapshots of the whole embryo 90 min before and 90 min after microlumen appearance. Scale bar, 10 µm. Bottom shows magnifications of the rectangles. Scale bar, 1 µm. (B) Coefficient of variation of Cdh1-GFP intensity along cell-cell contacts. 337 and 333 contacts from 24 embryos at -90 and +90 min compared to the time of microlumen appearance respectively. * for Student's t test at $p < 10^{-4}$. (C) Schematic diagram of chimera experiments. (D) Chimeric embryos composed of control mTmG (cyan) and control mG (magenta) cells or of control mG (cyan) and mCdh1 (red) cells. Scale bars, 10 µm.*

indicates that fluid accumulation is required for detaching cell-cell contacts and Cdh1 reorganization. While fluid accumulation may displace Cdh1, conversely, Cdh1 could provide mechanical resistance to fluid accumulation. Therefore, we patterned cell-cell adhesion to test if this could affect lumen expansion. To achieve this, we took advantage of embryos in which Cdh1 is knocked out maternally (mCdh1), which form a blastocyst despite their initially lower adhesion (*23, 25*). We generated chimeric embryos made either from two differently labeled control embryos or from control and mCdh1 embryos (Fig. 2C). Control chimeras formed their blastocoel on either half of the embryo (Fig. 2D). On the other hand, in mCdh1 chimeras, the blastocoel formed preferentially on the mCdh1 half (Fig. 2D). This affected the allocation of cells to the different tissues of the blastocyst (Fig. S8) with mCdh1 blastomeres contributing almost exclusively to the mural part of the

measured pressures of 296 ± 114 Pa (Mean ± SD) for 25 blastocysts (Fig. S6), which is about 10 times higher than for individual blastomeres (*23, 24*). This reveals that the hydrostatic pressure in the blastocyst is large and of magnitude comparable to pressures capable of inducing hydraulic fracturing in vitro (*21*). Therefore, fluid accumulation may be responsible for detaching cell-cell contacts and reorganizing Cdh1. To block fluid accumulation, we used three complementary treatments (Fig. S7). All three treatments prevented microlumen formation and Cdh1-GFP remained homogeneously distributed at cell-cell contacts (Fig. S7, Movies 3-5). This

4

TE, which is the TE that lines the blastocoel (Fig. S8). Therefore, patterning Cdh1 levels is sufficient to direct the accumulation of fluid. Altogether, we find that pressurized fluid collects along the path of lowest mechanical resistance, separates cell-cell contacts and reorganizes Cdh1 adhesion molecules. We therefore propose that microlumens form throughout the embryo by hydraulic fracturing of cell-cell contacts.

We then proceeded to investigate how the embryo resolves the hundreds of microlumens into one single blastocoel during the discharge phase. One mechanism would be for microlumens to coalesce and fuse when in close proximity. On time scales ranging from tens of minutes to hours, we could not observe frequent fusion events or movements of microlumens towards the final position of the blastocoel (Movies 1-2). We used light-sheet microscopy to image microlumens at high temporal and spatial resolution, and observed that microlumens seem to drain their content on time scales of few minutes (Movie 6). Indeed, microlumens are physically connected through the intercellular space as revealed by labeled dextran diluted in the culture medium that

builds up transiently at all cell-cell contacts during microlumen formation and then in the blastocoel (Movie 7). In fact, any difference in hydrostatic pressure between two connected microlumens should lead to a flow of luminal fluid from the more pressurized microlumen to its counterpart (Fig. 3A). The pressure in microlumens is related to the tension and curvature at the lumen interface via the Young-Laplace equation (Supp. Text). At same microlumen tension, a pressure difference is due to differences in microlumen sizes. This leads smaller microlumens to discharge into larger ones (Fig. 3A, Movie 8), and may explain why small bicellular microlumens shrink earlier than larger multicellular microlumens (Fig. 1B, Fig.S3). This process is reminiscent of Ostwald ripening (*26*), which drives the slow coarsening of foams. In the embryo, however, the exchange is not limited by diffusion but rather by fluid flow through the intercellular space. In addition, surface tension may not be homogeneous and, in fact, the direction of the flow may be reversed for a given asymmetry in tension between two lumens (Fig. 3A). To study microlumen dynamics, we modeled the embryo as a 2D network of pressurized
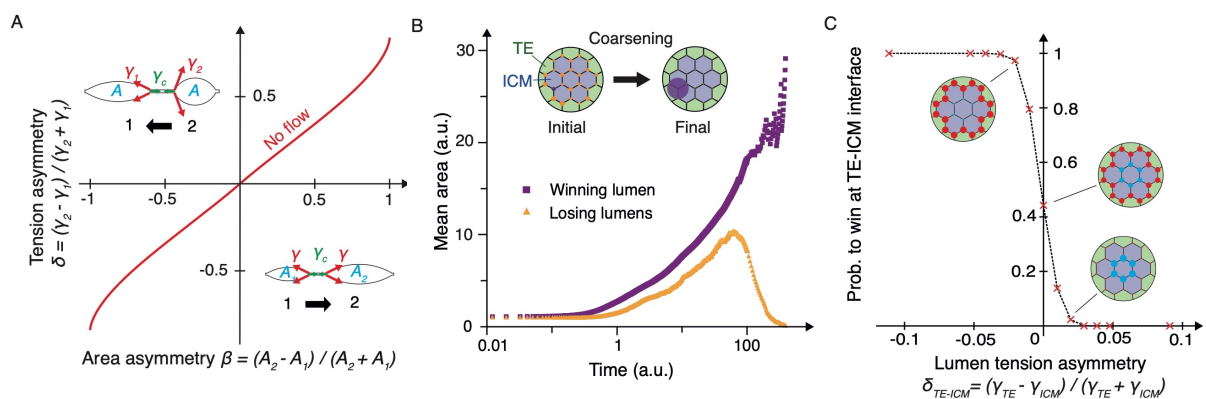

Figure 3: physical model of lumen coarsening and localization. (A) Phase diagram for the fluid flow between two lumens as a function of their tension asymmetry δ and area asymmetry β. Adhesive contact tension γ_c is 1 (Fig. S9). (B) Mean time evolution of the area of winning (purple squares) and losing lumens (orange triangles) resulting in the coarsening of the lumen network as depicted on the schematic diagram (50 simulations with γ_{TE} = 0.9, γ_{ICM} = 1, γ_c = 1, pumping rate $\lambda_p = 10^{-3}$ a.u.). (C) Winning probability for lumens at TE-ICM interfaces as a function of tension asymmetry δ_{TE-ICM}. Each point results from averaging over 1000 simulations ($\lambda_p = 10^{-3}$ a.u.). Insets show the mean localization of winning lumens.
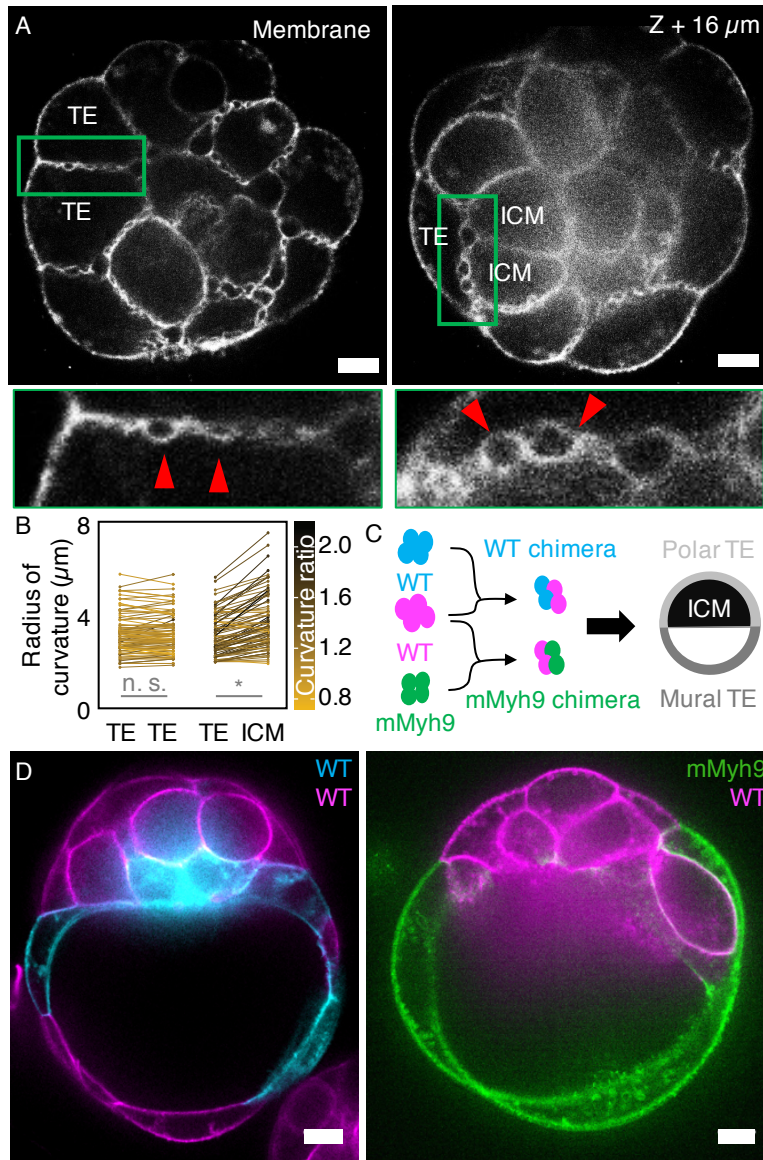
Figure 4: microlumen coarsening is controlled by cell contractility. (A) The curvature of microlumens is symmetric at TE-TE interfaces (left, arrowheads) and more asymmetric at TE-ICM interfaces (right image shows a confocal slice 16 µm deeper than the one above). Green squares are magnified 3 times on the bottom images. Scale bar, 10 µm. (B) Radius of curvature at microlumens facing TE-TE (71) and TE-ICM (58) interfaces from 7 embryos during the discharge phase, 60 min after inversion. The ratio of curvature is color-coded with TE cells ordered randomly for TE-TE ratios. * for paired Student's t test at $p < 10^{-7}$, n. s. for not significant with $p > 10^{-2}$. (C) Schematic diagram of chimera experiments. (D) Chimeric embryos composed of control mTmG (cyan) and control mG (magenta) cells or of control mG (magenta) and mCdh1 (green) cells. Scale bars, 10 µm.

microlumens and performed numerical simulations to predict the position of the final lumen (Fig. 3B-C). The size of a microlumen evolves by direct swelling and via fluid exchange through the network (Fig. 3B, Supp. Text). As observed experimentally (Fig. 1B, Fig. S3), lumens show a swelling phase followed by a discharge of all lumens but one, which siphons all the fluid (Fig. 3B-C, Movie 8). This biphasic signature is characteristic of a coarsening mechanism akin to Ostwald ripening (Supp. Text) (*26*).

In networks with homogeneous lumen tension, the lower connectivity of microlumens at the border favors the formation of the final lumen in the interior (Fig. 3C, Supp. Text). In agreement with

mCdh1 chimera experiments (Fig. 2D), the model predicts that a pattern of adhesive contact tension could be sufficient to position the blastocoel at the TE-ICM interface (Fig. S9). Alternatively, when microlumens in the interior are imposed a small excess in tension, the final lumen ends up invariably at the margin (Fig. 3C). The model predicts hence that higher lumen tension at the ICM-ICM interface is sufficient to position the blastocoel between TE and ICM cells, as observed in vivo.

To examine whether differences in surface tension between blastomeres could explain how coarsening directs luminal fluid towards the TE-ICM interface, we first investigated the shape of microlumens. When measuring

the radius of curvature of microlumens, we detect asymmetries, which are more pronounced at heterotypic TE-ICM interfaces compared to those at homotypic TE-TE interfaces (Mean ± SEM, curvature ratio of 1.01 ± 0.02 for 71 TE-TE microlumens and 1.25 ± 0.04 for 58 TE-ICM microlumens from 7 embryos, Student t test p < 10^{-2}, Fig. 4A-B, Movie 1). Moreover, microlumens at TE-ICM interfaces bulge into the TE cell in most cases rather than into ICM cells (79% of 58 microlumens from 7 embryos, Chi squared p < 10^{-3}). This suggests differences in the hydrostatic pressure and/or surface tension between TE and ICM cells. Such differences are supported by the cell-scale curvature of TE-ICM interfaces, where ICM cells bulge into TE cells (Fig. S10). This disparity is likely due to higher contractility of ICM cells compared to TE cells, which is responsible for their sorting at the 16-cell stage (*24*). Indeed, inhibiting cell contractility decreases the curvature at TE-ICM interfaces (Fig. S10) and the surface tension of the blastocyst (Fig. S6). Our model predicts that this pattern of contractility within the embryo would result in microlumens preferentially discharging to the TE-ICM interface (Fig. 3C, Movie 9).

To experimentally test the ability for heterogeneous contractility to direct the offloading of microlumens, we generated chimeras (Fig. 4C) using embryos in which Myh9 is maternally knocked out (mMyh9), which are viable despite their lower levels of Myh9 and lower surface tension (*24*). As previously (Fig. 2C-D), control chimeras form their blastocoel on either side of the embryo (Fig. 4D). On the other hand, in mMyh9 chimeras, the blastocoel forms preferentially on the mMyh9 half (Fig. 4D). This affects the allocation of cells to the different tissues of the blastocyst (Fig. S8). In agreement with previous analogous experiments (*24*), mMyh9 blastomeres are

depleted from the ICM and, instead, contribute mostly to the mural TE (Fig. S8). Therefore, differences in Myh9 levels are sufficient to control the position of the blastocoel, in agreement with corresponding simulations (Movie 10). Altogether, we propose that a mechanism akin to Ostwald ripening directs the offloading of luminal fluid into the blastocoel.

We have established that both patterned cell-cell adhesion and patterned cell contractility can position the blastocoel (Fig. 2D, 4D). This suggests that both localized hydraulic fracturing of cell-cell contacts and directed fluid offloading could set the first axis of symmetry of the mouse embryo. These two phenomena constitute complementary mechanisms explaining the formation and positioning of lumens in general, and of basolateral lumens in particular, which can be found in healthy (*27*) and pathological situations (*12*). As far as the blastocyst is concerned, although both hydraulic fracturing and active coarsening can position the blastocoel, we are unable to detect any conclusive relation between the final position of the blastocoel and the initial localization of Cdh1 or contact fracture (Fig. S4-5, S11). On the other hand, differences in contractility are undoubtedly at play (*24*, *28*, *29*) (Fig. 4, Fig. S10). Therefore, we propose that the first axis of symmetry of the mouse embryo is positioned by contractility-mediated ripening of microlumens formed after hydraulic fracturing of cell-cell contacts.

Determining the molecular and mechanical events controlling the formation of microlumens and the fracture of cell-cell contacts constitutes exciting new research avenues, which will greatly benefit from previous studies on contact mechanical stability (*21*, *30*). Finally, to build a comprehensive model of blastocoel formation, future studies will need to integrate explicitly individual cell mechanics

and to evaluate the contributions of other cellular processes such as vesicular trafficking (*15*) and ion exchange (*8*).

References

1. J.-L. Maître, Mechanics of blastocyst morphogenesis. *Biol Cell.* **109**, 323–338 (2017).

2. J. Rossant, Making the Mouse Blastocyst: Past, Present, and Future. *Curr Top Dev Biol.* **117**, 275–288 (2016).

3. Y. Marikawa, V. B. Alarcon, Creation of trophectoderm, the first epithelium, in mouse preimplantation development. *Results Probl Cell Differ.* **55**, 165–184 (2012).

4. K. Takaoka, H. Hamada, Cell fate decisions and axis determination in the early mouse embryo. *Development.* **139**, 3–14 (2012).

5. Y. Kurotaki, K. Hatta, K. Nakao, Y.-I. Nabeshima, T. Fujimori, Blastocyst axis is specified independently of early cell lineage but aligns with the ZP shape. *Science.* **316**, 719–723 (2007).

6. A. J. Blasky, A. Mangan, R. Prekeris, Polarized protein transport and lumen formation during epithelial tissue morphogenesis. *Annu Rev Cell Dev Biol.* **31**, 575–591 (2015).

7. Q. Li *et al.*, Extracellular matrix scaffolding guides lumen elongation by inducing anisotropic intercellular mechanical tension. *Nat Cell Biol.* **18**, 311–318 (2016).

8. S. Dasgupta, K. Gupta, Y. Zhang, V. Viasnoff, J. Prost, Physics of lumen growth. *Proc Natl Acad Sci USA.* **115**, E4751–E4757 (2018).

9. M. N. Shahbazi *et al.*, Pluripotent state transitions coordinate morphogenesis in mouse and human embryos. *Nature.* **552**, 239–243 (2017).

10. B. Strilić *et al.*, Electrostatic cell-surface repulsion initiates lumen formation in developing blood vessels. *Curr Biol.* **20**, 2003–2009 (2010).

11. A. Z. Wang, G. K. Ojakian, W. J. Nelson, Steps in the morphogenesis of a polarized epithelium. I. Uncoupling the roles of cell-cell and cell-substratum contact in establishing plasma membrane polarity in multicellular epithelial (MDCK) cysts. *J Cell Sci.* **95 (Pt 1)**, 137–151 (1990).

12. O. Zajac *et al.,* Tumour spheres with inverted polarity drive the formation of peritoneal metastases in patients with hypermethylated colorectal carcinomas. *Nat Cell Biol.* **20**, 296–306 (2018).

13. K. Kono, D. A. A. Tamashiro, V. B. Alarcon, Inhibition of RHO-ROCK signaling enhances ICM and suppresses TE characteristics through activation of Hippo signaling in the mouse blastocyst. *Dev Biol.* **394**, 142–155 (2014).

14. C. L. Garbutt, J. C. Chisholm, M. H. Johnson, The establishment of the embryonic-abembryonic axis in the mouse embryo. *Development.* **100**, 125–134 (1987).

15. L. M. Wiley, M. A. Eglitis, Effects of colcemid on cavitation during mouse blastocoele formation. *Exp Cell Res.* **127**, 89–101 (1980).

16. J. E. Fléchon, M. Panigel, D. C. Kraemer, S. S. Kalter, E. S. Hafez, Surface ultrastructure of preimplantation baboon embryos. *Anat. Embryol.* **149**, 289–295 (1976).

17. P. R. Hurst, K. Jefferies, P. Eckstein, A. G. Wheeler, An ultrastructural study of preimplantation uterine embryos of the rhesus monkey. *J. Anat.* **126**, 209–220 (1978).

18. M. D. Muzumdar, B. Tasic, K. Miyamichi, L. Li, L. Luo, A global double-fluorescent Cre reporter mouse. *genesis.* **45**, 593–605 (2007).

19. L. Larue, M. Ohsugi, J. Hirchenhain, R. Kemler, E-cadherin null mutant embryos fail to form a trophectoderm epithelium. *Proc Natl Acad Sci U S A.* **91**, 8263–8267 (1994).

20. I. Poser *et al.,* BAC TransgeneOmics: a high-throughput method for exploration of

protein function in mammals. *Nat Methods.* **5**, 409–415 (2008).

21. L. Casares *et al.*, Hydraulic fracture during epithelial stretching. *Nat Materials.* **14**, 343–351 (2015).

22. K. Guevorkian, J. L. Maitre, Micropipette aspiration: A unique tool for exploring cell and tissue mechanics in vivo. *Methods Cell Biol.* **139**, 187–201 (2017).

23. J.-L. Maître, R. Niwayama, H. Turlier, F. Nédélec, T. Hiiragi, Pulsatile cell-autonomous contractility drives compaction in the mouse embryo. *Nat Cell Biol.* **17**, 849–855 (2015).

24. J.-L. Maître *et al.*, Asymmetric division of contractile domains couples cell positioning and fate specification. *Nature.* **536**, 344–348 (2016).

25. R. O. Stephenson, Y. Yamanaka, J. Rossant, Disorganized epithelial polarity and excess trophectoderm cell fate in preimplantation embryos lacking E-cadherin. *Development.* **137**, 3383–3391 (2010).

26. W. Ostwald, Über die vermeintliche Isomerie des roten und gelben Quecksilberoxyds und die Oberflächenspannung fester Körper. *Z Phys Chem.* **34**, 495–503 (1900).

27. T. Kučera *et al.*, Ancestral vascular lumen formation via basal cell surfaces. *PLoS ONE.* **4**, e4132 (2009).

28. S. Anani, S. Bhat, N. Honma-Yamanaka, D. Krawchuk, Y. Yamanaka, Initiation of Hippo signaling is linked to polarity rather than to cell position in the pre-implantation mouse embryo. *Development.* **141**, 2813–2824 (2014).

29. C. R. Samarage *et al.*, Cortical Tension Allocates the First Inner Cells of the Mammalian Embryo. *Dev Cell.* **34**, 435–447 (2015).

30. J. L. Maitre *et al.*, Adhesion Functions in Cell Sorting by Mechanically Coupling the Cortices of Adhering Cells. *Science.* **338**, 253–256 (2012).

31. S. Machado, V. Mercier, N. Chiaruttini, LimeSeg: a coarse-grained lipid membrane simulation for 3D image segmentation. *BMC Bioinformatics.* **20**, 2 (2019).

32. L. C. Barcroft, H. Offenberg, P. Thomsen, A. J. Watson, Aquaporin proteins in murine trophectoderm mediate transepithelial water movements during cavitation. *Dev Biol.* **256**, 342–354 (2003).

33. L. M. Wiley, Cavitation in the mouse preimplantation embryo: Na/K-ATPase and the origin of nascent blastocoele fluid. *Dev Biol.* **105**, 330–342 (1984).

34. W. N. de Vries *et al.*, Expression of Cre recombinase in mouse oocytes: a means to study maternal effect genes. *genesis.* **26**, 110–112 (2000).

35. O. Boussadia, S. Kutsch, A. Hierholzer, V. Delmas, R. Kemler, E-cadherin is a survival factor for the lactating mouse mammary gland. *Mech Dev.* **115**, 53–62 (2002).

36. J. Jacobelli *et al.*, Confinement-optimized three-dimensional T cell amoeboid motility is modulated via myosin IIA-regulated adhesions. *Nat Immunol.* **11**, 953–961 (2010).

37. G. Testa *et al.*, Engineering the mouse genome with bacterial artificial chromosomes to create multipurpose alleles. *Nat Biotechnol.* **21**, 443–447 (2003).

38. J. D. Biggers, L. K. McGinnis, M. Raffin, Amino Acids and Preimplantation Development of the Mouse in Protein-Free Potassium Simplex Optimized Medium. *Biol Reprod.* (2000).

39. J. Schindelin *et al.*, Fiji: an open-source platform for biological-image analysis. *Nat Methods.* **9**, 676–682 (2012).

40. V. M. R. Muggeo, Estimating regression models with unknown break-points. *Stat Med.* **22**, 3055–3071 (2003).

41. V. M. R. Muggeo, segmented: An R Package to Fit Regression Models with Broken-Line Relationships. *R News.* **8**, 20–25 (2008).

42. Miyaguchi, K. Ultrastructure of the zonula adherens revealed by rapid-freeze deep-etching. *J Struct Biol* 132, 169–178 (2000).
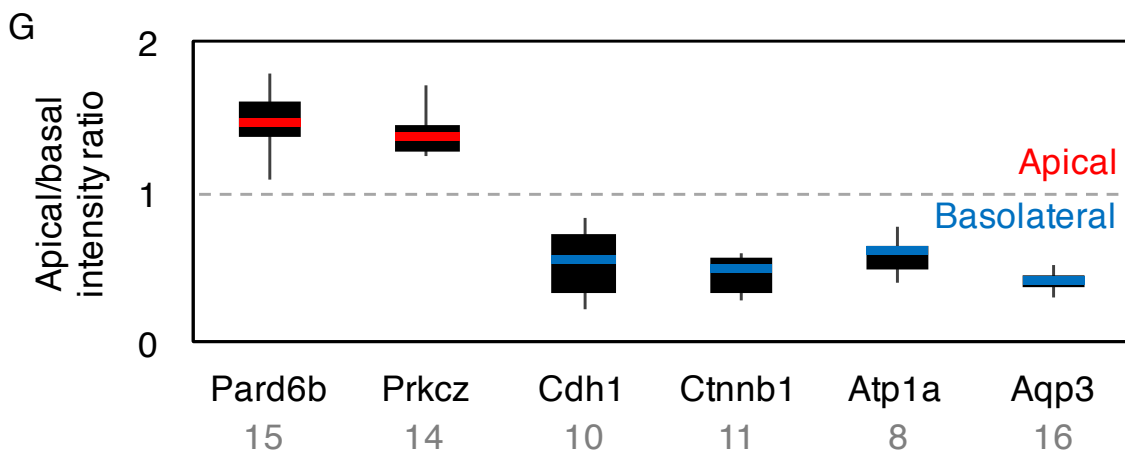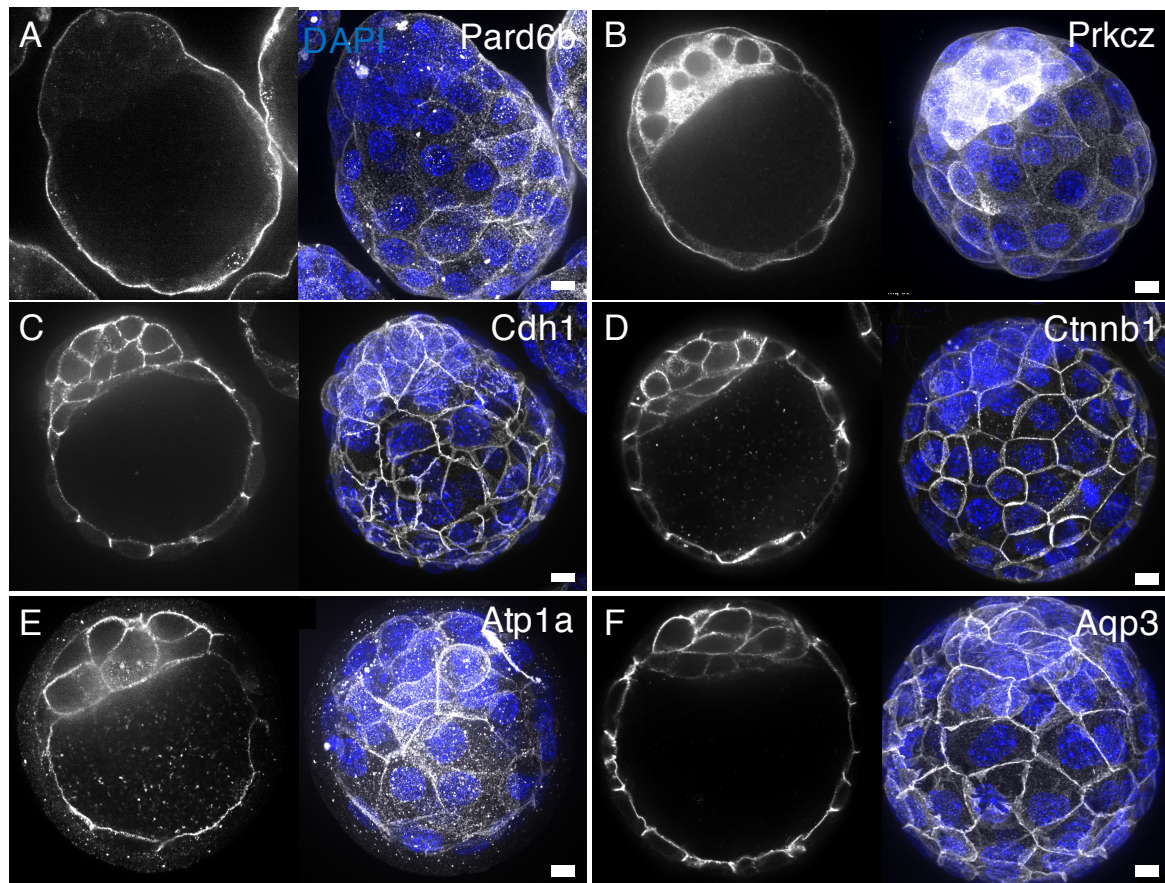
Supplementary Figure 1: blastocyst form the blastocoel on the basolateral interface of cells.

(A-D) Immunostaining (grey) showing single confocal slices (left) and maximum projections (right) with nuclei stained with DAPI (blue).

(A-B) Apical markers Pard6b and Prkcz (aPKCζ).

(C-D) Basolateral markers Cdh1 (E-cadherin), Ctnnb1 (β-catenin), Atp1a (the ATPase subunit of the Na/K pump), Aqp3 (Aquaporin3).

(G) Apical to basal intensity ratio for 3 mural TE cells from 15/14/10/11/8/16 embryos for Pard6b, Prkcz, Cdh1, Ctnnb1, Atp1a, Aqp3 respectively.
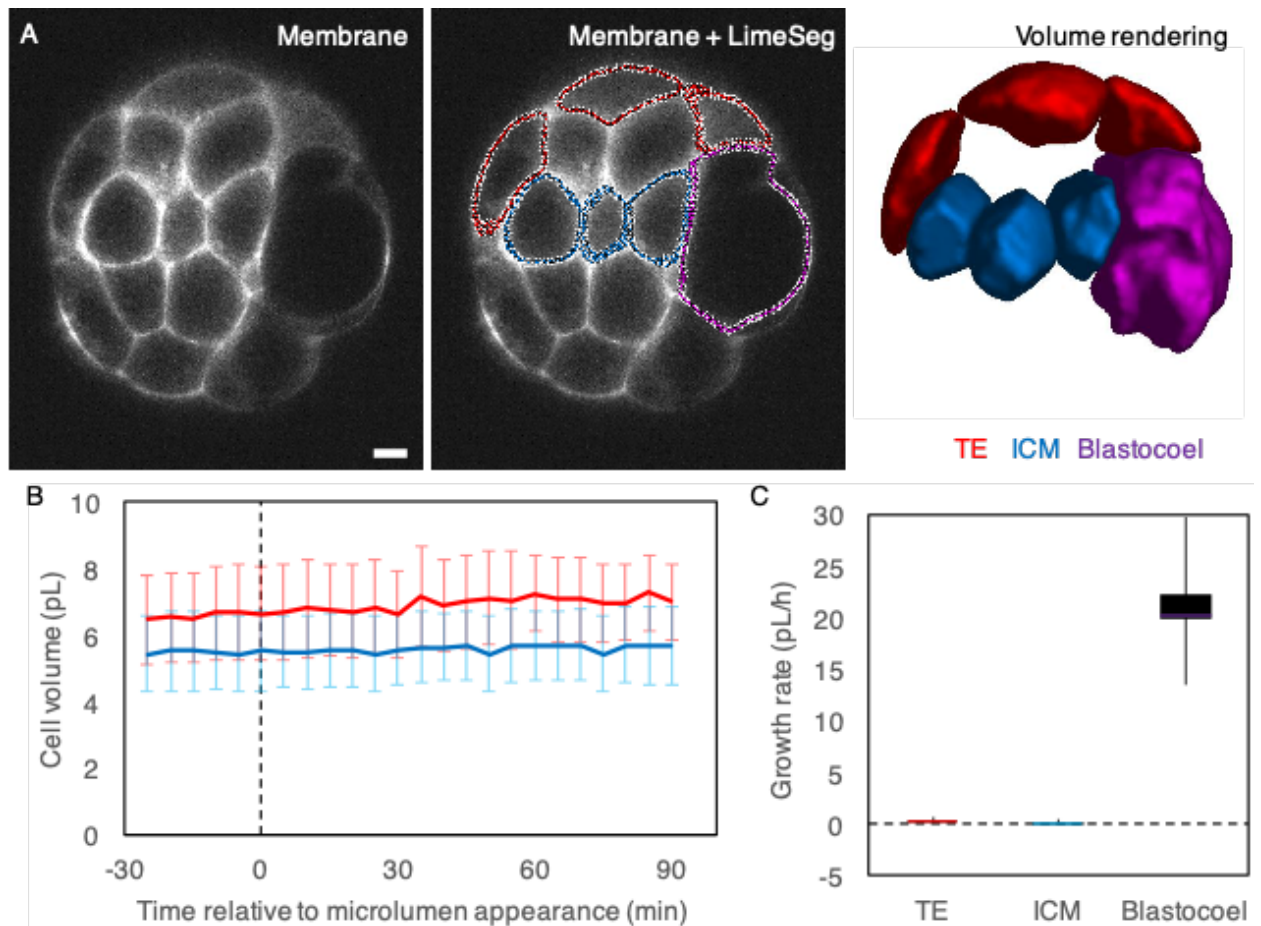
Supplementary Figure 2: cell volume remains constant during microlumen formation and coarsening.

(A) Typical example from confocal imaging of mTmG embryos using the light sheet microscope (left), with the result of segmentation using LimeSeg (middle and right) (*31*). (B) Mean ± SEM volume of 15 TE (red) and 15 ICM (blue) cells from 5 embryos. (C) Growth rate of the blastocoel (purple) and, 15 TE (red) and 15 ICM (blue) cells from 5 embryos. Measurements were performed during microlumen formation and coarsening, which corresponds to the initially slow growth of the blastocoel (Fig. 1).
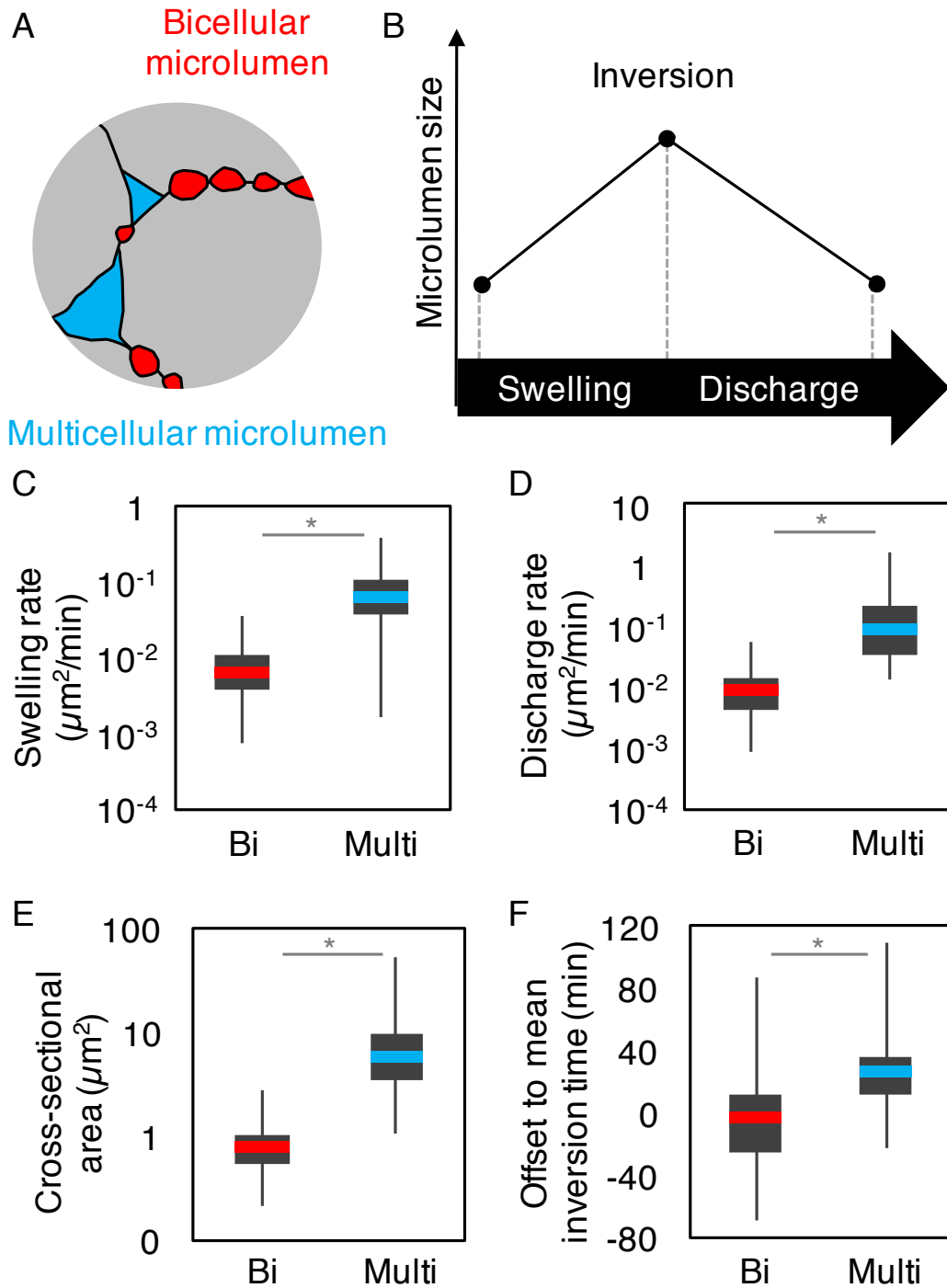
Supplementary Figure 3: microlumen dynamics at bi-cellular and multicellular interfaces.
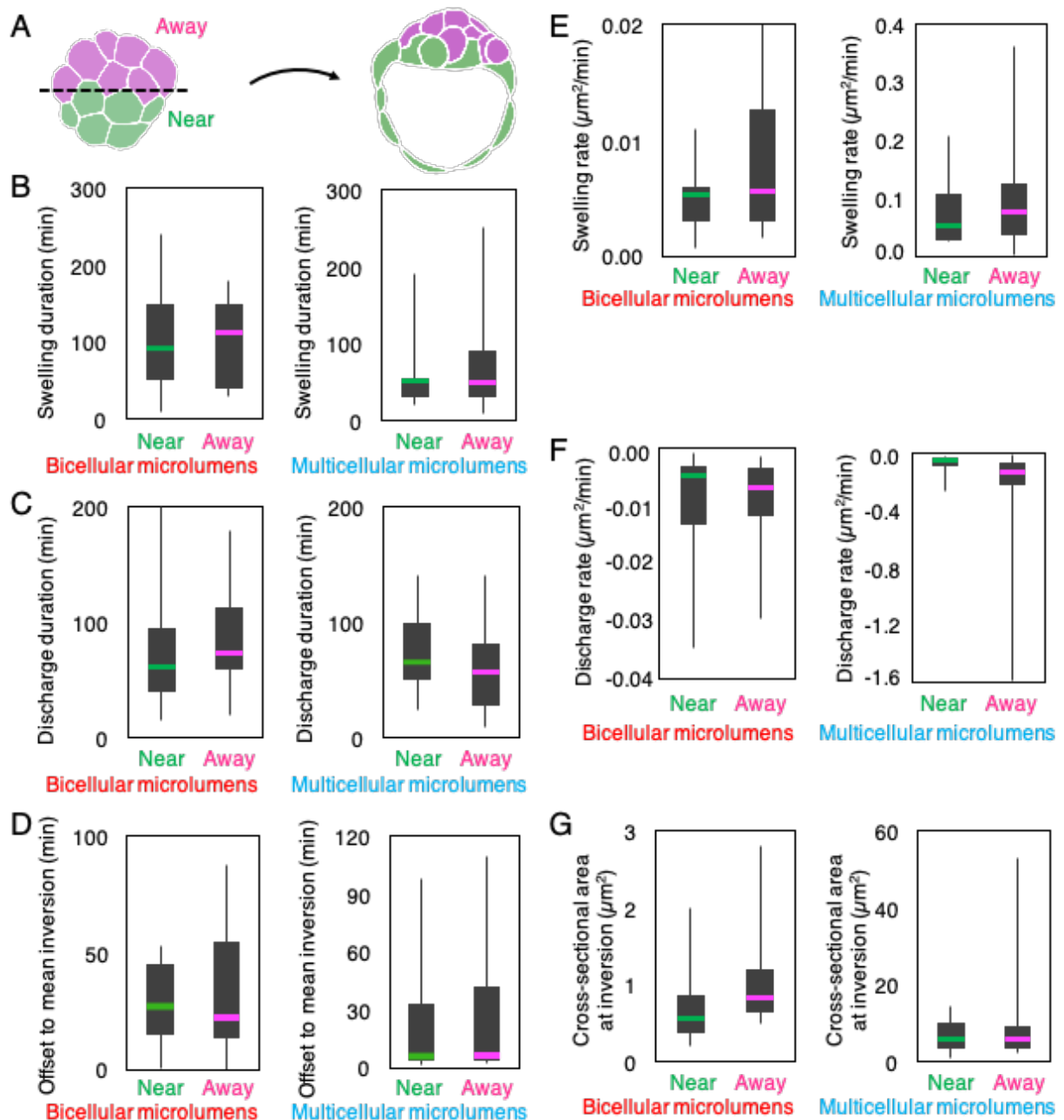
(A) Schematic diagram of the different microlumen types: bicellular (red) and multicellular (blue). (B) Schematic diagram of the two phases of microlumen lifetime.

(C-F) Swelling (C) and shrinkage (D) rates, cross-sectional area at the time of inversion (E), and offset to mean inversion time (F) for microlumens at 35 bicellular and 21 multicellular junctions from 7 embryos. (C-E) display data on a log scale. * for Student's *t* test at p < 10^{-2}.
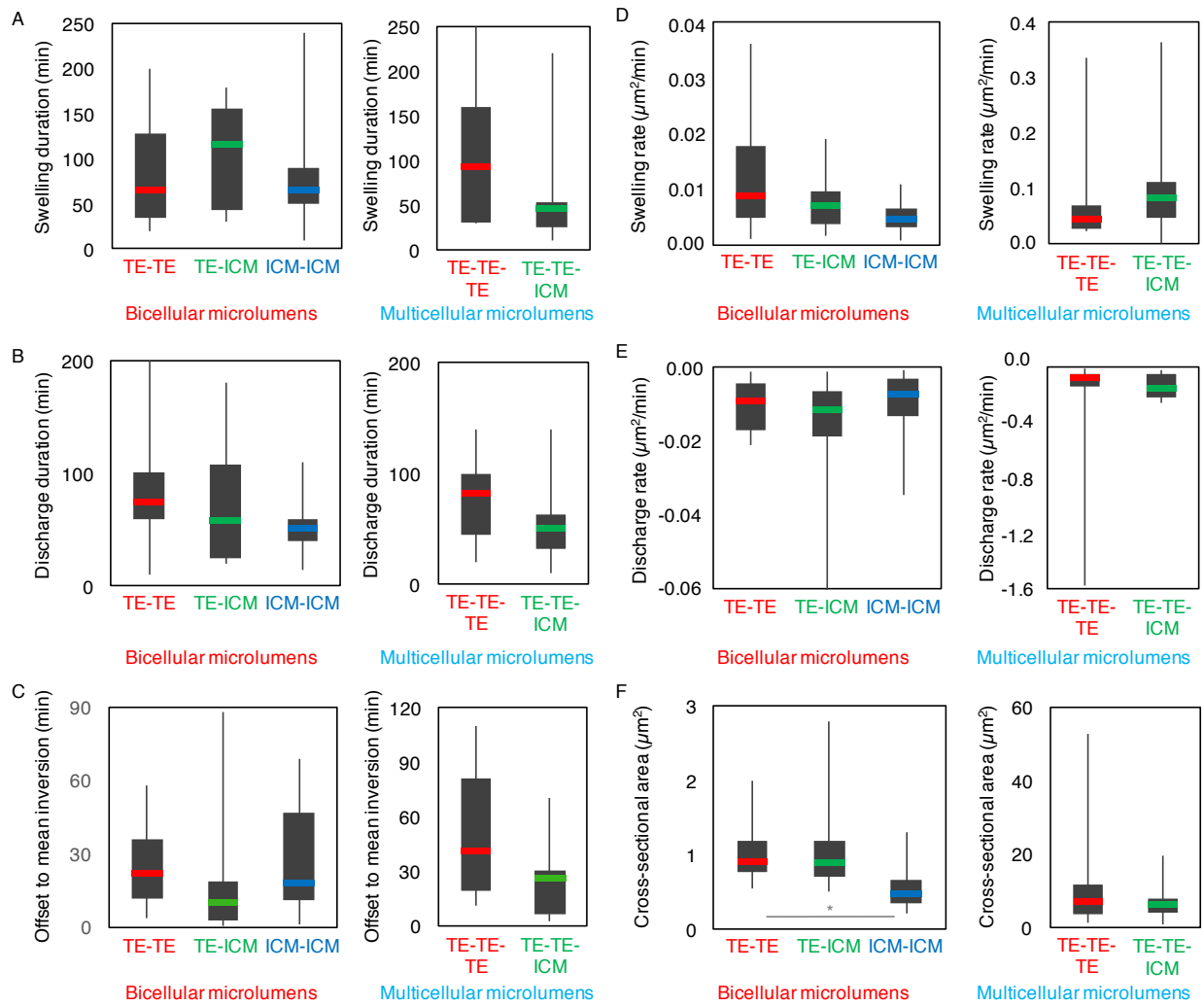
Supplementary Figure 4: microlumen growth dynamics at TE or ICM interfaces.
(A-F) Swelling (A) and discharge duration (B), offset to mean inversion time (C), swelling (D) and discharge rate (E), and cross-sectional area (F) for bicellular microlumens at 12 TE-TE, 10 TE-ICM, 13 ICM-ICM interfaces and for multicellular microlumens at 8 TE-TE-TE and 11 TE-TE-ICM junctions from 7 embryos. Student's t test at $p > 10^{-2}$ gives no significant differences.

Supplementary Figure 5: microlumen growth dynamics in respect of the eventual lumen position.

(A) Schematic diagram of the location of the measurements of microlumen dynamics.

(B-G) Swelling (B) and discharge duration (C), offset to mean inversion time (D), swelling (E) and discharge rate (F), and microlumen cross-sectional area (G) for interfaces near (N = 13) or away (N = 12) from the final position of the blastocoel in 5 embryos for bicellular microlumens and for interfaces near (N = 9) or away (N = 12) from the final position of the blastocoel in 7 embryos for multicellular microlumens. Student's t test at $p > 10^{-2}$ gives no significant differences.
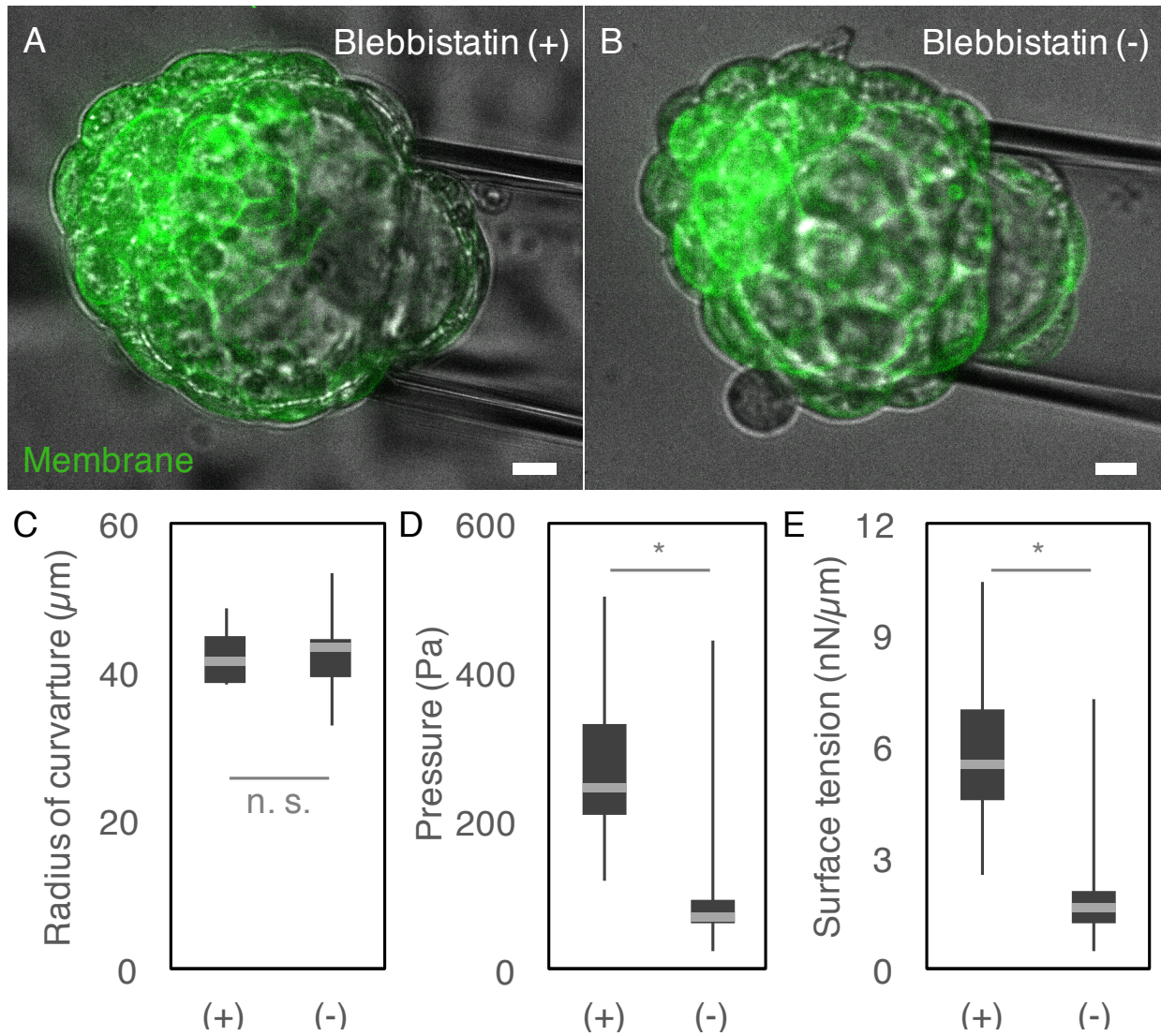
Supplementary Figure 6: hydrostatic pressure and surface tension of the blastocyst are controlled by actomyosin contractility.

(A-B) Blastocyst microaspiration on the mural TE in the presence of 25 μM inactive enantiomere Blebbistatin (+) or active enantiomere Blebbistatin (-). Brighfield in grey and membrane (mTmG) in green. Scale bar, 10 μm.

(C-E) Radius of curvature of the mural TE, hydrostatic pressure and surface tension of 25 (+) and 24 (-) blastocysts. * for Student's t test at $p < 10^{-6}$, n. s. for not significant with $p > 10^{-2}$.
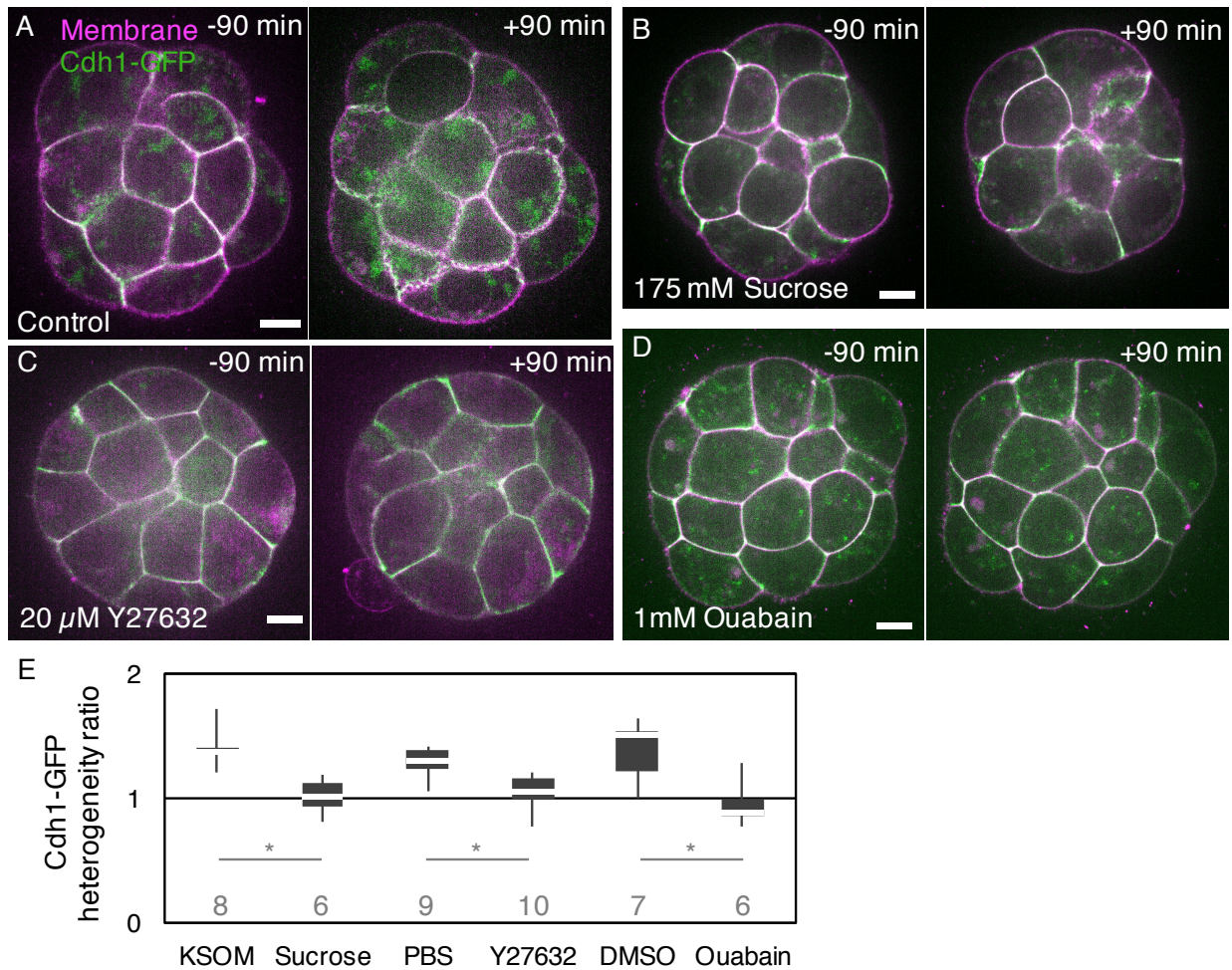
Supplementary Figure 7: fluid accumulation is required for Cdh1-GFP rearrangement.
(A-D) Cdh1-GFP (green) and membrane (magenta) for embryos in control medium (A), 175 mM sucrose (B), 20 μM Y27632 (C) or 1 mM Ouabain (D) containing medium. Scale bar, 10 μm. Sucrose blocks fluid pumping by overriding the osmotic gradient built by the embryo (*32*). Y27632 inhibits Rock, which disrupts apicobasal polarity and polarized fluid transport towards the intercellular space (*13*). Ouabain inhibits the Na/K pump, which contributes to building the osmotic gradient (*33*).
(E) Quantification of Cdh1-GFP signal reorganisation along cell-cell contacts. The ratio of coefficient of variation is calculated between 90 min before and 90 min after the appearance of microlumens in control embryos and at the time of the latest control embryo from the same experiment in sucrose, Y27632 and Ouabain treated embryos. KSOM (254 contacts from 8 embryos) was used as control for sucrose (251 contacts from 6 embryos) experiments. PBS (263 contacts from 9 embryos) was added for control of Y27632 (298 contacts from 10 embryos) experiments. DMSO (153 contacts from 7 embryos) was added for Ouabain (136 contacts from 6 embryos) experiments. * for Student's t test at p < 10^{-2}.
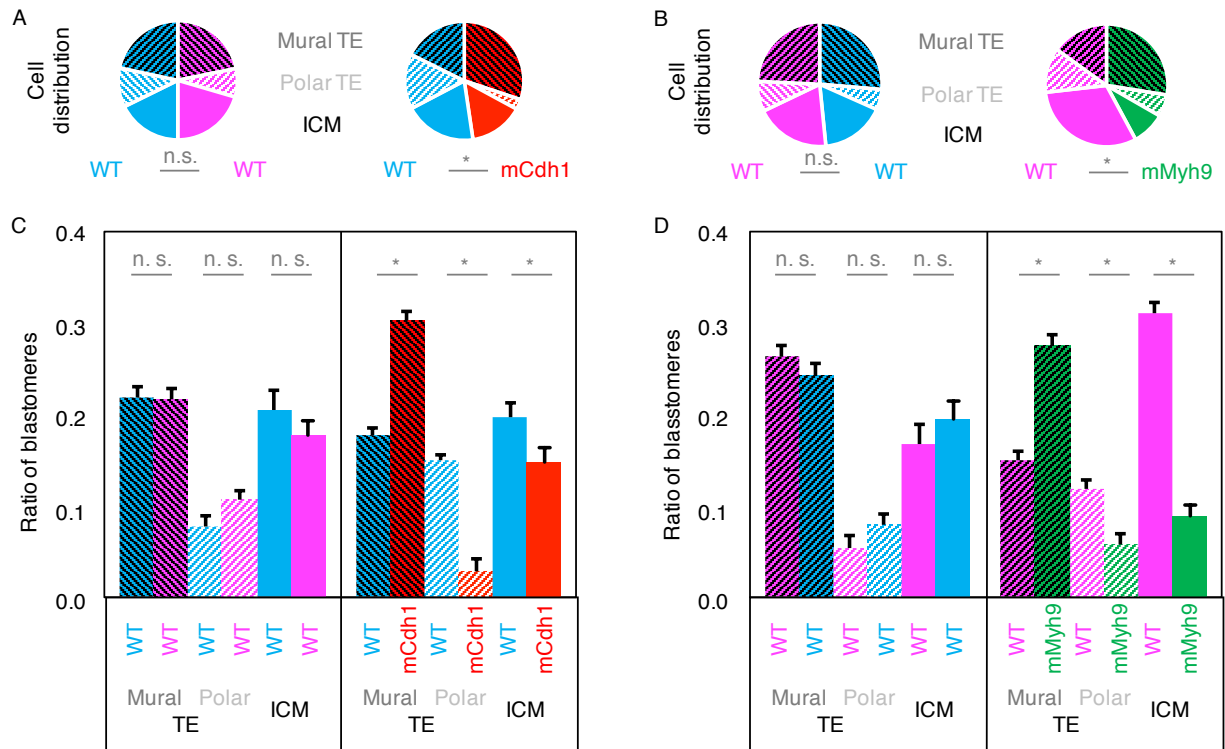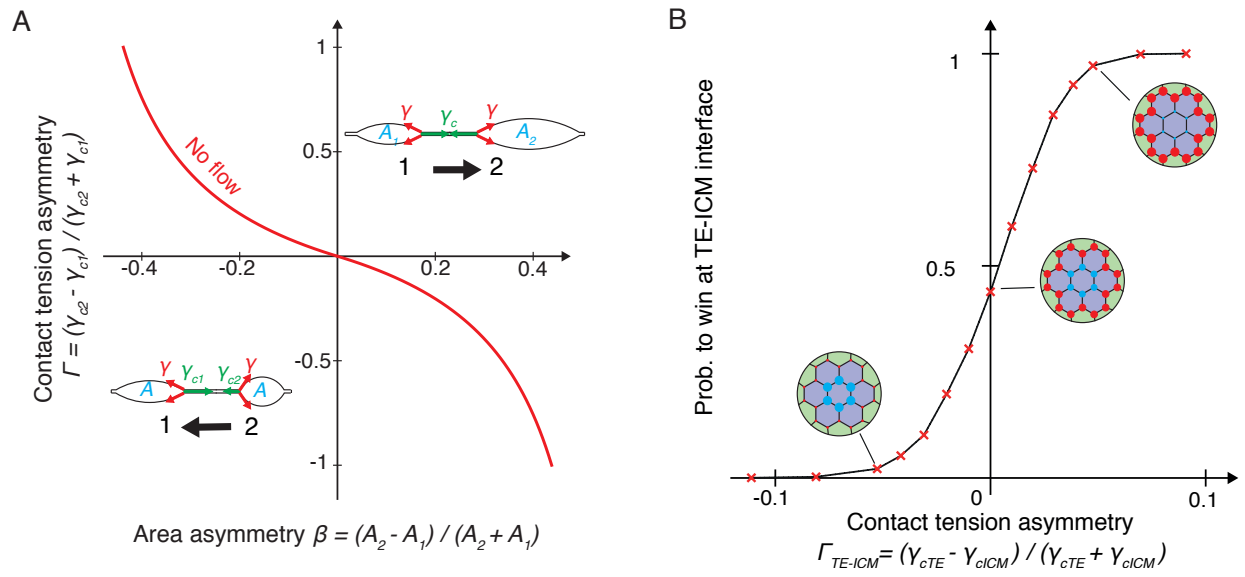
Supplementary Figure 8: cell distribution in chimeric embryos.

(A-D) Distribution of cells in 22 control and 33 mCdh1 mutant chimeras and in 25 control and 28 mMyh9 mutant chimeras. Proportion of WT or mutant cells in the mural (dark stripes) or polar (clear stripes) TE, or in the ICM (plain).

(A-B) Distribution heterogeneity between genotypes within each types of chimera is compared using Chi-squared test, * for $p < 10^{-2}$, n. s. for not significant with $p > 10^{-2}$.

(C-D) Mean ± SEM contribution of each genotype to mural (dark stripes) or polar (clear stripes) TE, or to ICM (plain). * for Mann-Whitney U test at $p < 10^{-3}$, n.s. for not significant at $p > 10^{-2}$.

A

Contact tension asymmetry $\Gamma = (\gamma_{c2} - \gamma_{c1}) / (\gamma_{c2} + \gamma_{c1})$

No flow

Area asymmetry $\beta = (A_2 - A_1) / (A_2 + A_1)$

B

Prob. to win at TE-ICM interface

Contact tension asymmetry $\Gamma_{TE-ICM} = (\gamma_{cTE} - \gamma_{cICM}) / (\gamma_{cTE} + \gamma_{cICM})$

Supplementary Figure 9: effect of adhesive contact tension on lumen coarsening and localization.

(A) Phase diagram for the fluid flow between two lumens as function of the adhesive contact tension asymmetry $\Gamma = (\gamma_{c2} - \gamma_{c1}) / (\gamma_{c1} + \gamma_{c2})$ and initial size asymmetry $\beta = (A_2 - A_1) / (A_1 + A_2)$. Lumen tension γ is 1.

(B) Winning probability for lumens at TE-ICM interfaces as a function of the adhesive contact tension asymmetry $\Gamma_{TE-ICM} = (\gamma_{cTE} - \gamma_{cICM}) / (\gamma_{cTE} + \gamma_{cICM})$. Each point results from averaging over 1000 simulations ($\gamma_{TE} = \gamma_{ICM} = 1$, pumping rate $\lambda_p = 10^{-3}$ a.u.). Insets show the mean localization of winning lumens.

18
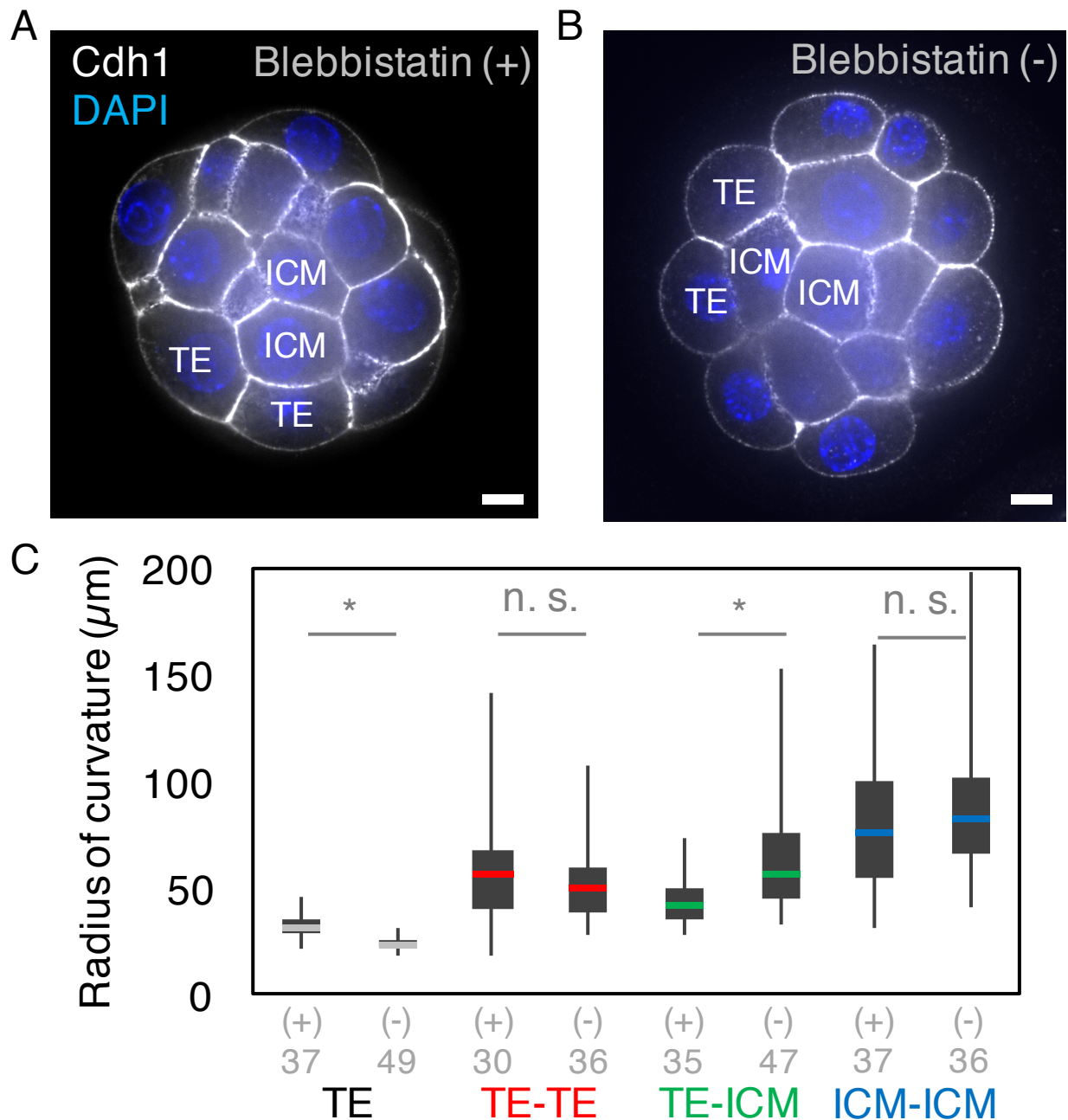
Supplementary Figure 10: different contractility of TE and ICM cells curve TE-ICM interfaces.

(A-B) 32-cell stage embryos before lumen formation in 25 μM inactive enantiomere Blebbistatin (+) or active enantiomere Blebbistatin (-). Scale bar, 10 μm.

(C) Radius of curvature at TE-TE, TE-ICM and ICM-ICM interfaces, and TE interfaces with the medium of 8 Blebbistatin (+) and 9 Blebbistatin (-) treated embryos. The number of interfaces is indicated. * for Student's t test at $p < 10^{-3}$, n. s. for not significant with $p > 10^{-2}$.
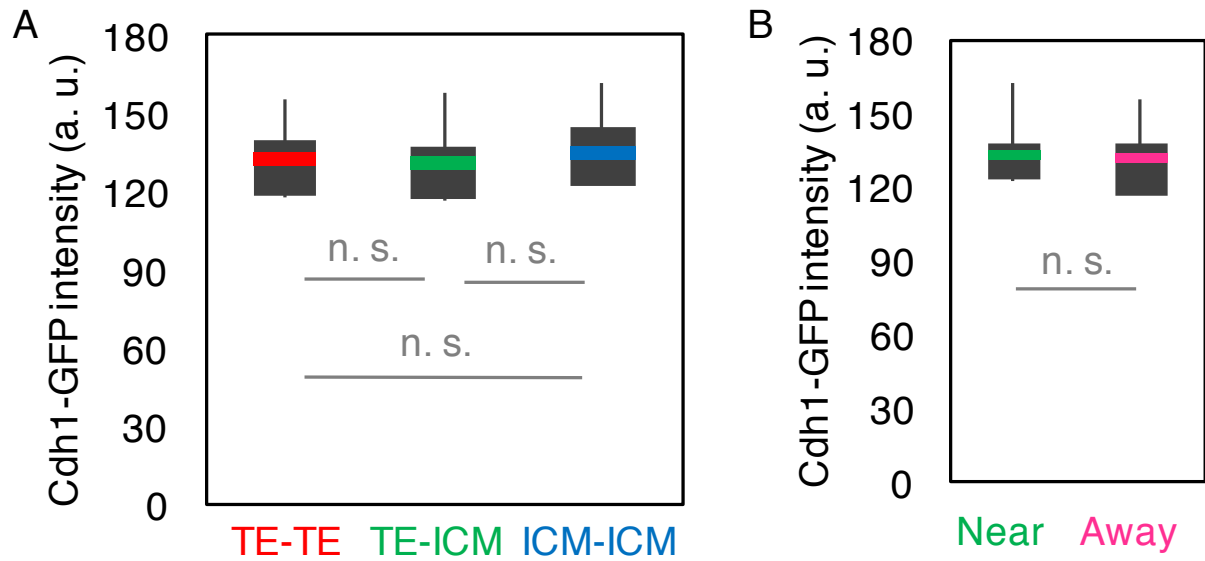
Supplementary Figure 11: adhesion is homogeneous throughout the embryo.

(A) Mean Cdh1-GFP intensity at 21 TE-TE, 34TE-ICM and 8 ICM-ICM interfaces from 10 embryos. Student's t test at $p > 10^{-2}$ gives no significant differences.

(B) Mean Cdh1-GFP intensity at cell-cell contacts near (N = 33) or away (N = 30) from the final position of the blastocoel in 10 embryos. Student's t test at $p > 10^{-2}$ gives no significant differences.

Movie 1: swelling and shrinkage of microlumens during blastocoel formation.
Single confocal slice of a timelapse of blastocoel formation in a mTmG embryo showing plasma membrane labelling. Images taken every 10 minutes, scale bar 10 μm. Time is set relative to the time of appearance of the first microlumens. Magenta asterisk marks the blastocoel, blue arrowheads point at multicellular microlumens and red arrowheads at bicellular microlumens.

Movie 2: Cdh1 reorganization during microlumen formation.
Timelapse of blastocoel formation in a Cdh1-GFP; mTmG embryo showing Cdh1 (green) and plasma membrane (magenta) labelling on two confocal slices separated by 20 μm. Images taken every 30 minutes, scale bar 10 μm. Magenta asterisk marks the blastocoel, blue arrowheads point at multicellular microlumens and red arrowheads at bicellular microlumens.

Movie 3: Rock inhibition prevents microlumen formation and Cdh1 reorganization.
Single confocal slice of a timelapse of blastocoel formation in a Cdh1-GFP; mTmG embryo showing Cdh1 (green) and plasma membrane (magenta) labelling in the presence of 20 μM Y27632. Images taken every 30 minutes, scale bar 10 μm.

Movie 4: hyperosmosis prevents microlumen formation and Cdh1 reorganization.
Single confocal slice of a timelapse of blastocoel formation in a Cdh1-GFP; mTmG embryo showing Cdh1 (green) and plasma membrane (magenta) labelling in the presence of 175 mM sucrose. Images taken every 30 minutes, scale bar 10 μm.

Movie 5: Na/K pump inhibition prevents microlumen formation and Cdh1 reorganization.
Single confocal slice of a timelapse of blastocoel formation in a Cdh1-GFP; mTmG embryo showing Cdh1 (green) and plasma membrane (magenta) labelling in the presence of 1 mM Ouabain. Images taken every 30 minutes, scale bar 10 μm.

Movie 6: high resolution imaging of the dischaege of microlumens.
Projection of confocal slices of a timelapse of blastocoel formation in a mTmG embryo showing plasma membrane labelling. The central microlumen expands as microlumens from neighbouring cell-cell interfaces shrinkage. Images taken every 5 s, scale bar 10 μm.

Movie 7: high resolution imaging of fluid accumulation.
Single confocal slices of a timelapse of blastocoel formation in a mTmG embryo showing plasma membrane labelling (cyan) growing in a medium containing a 3 kDa Dextran coupled to Alexa 488 (red). Placing embryos into Dextran containing medium before the sealing of tight junctions ensures that it is trapped in the intercellular space. Labelled dextran accumulates transiently at all cell-cell contacts during microlumen formation and then in the blastocoel. Accumulation of labelled dextran at contacts between ICM cells indicate that intercellular space is connected. Images taken every 2 min, scale bar 10 μm.

Movie 8: simulation of two lumens exchanging fluid through a pipe.
Both simulations have the same area asymmetry ($A_2 = 2A_1$) but lumen tension is either symmetric $\gamma_1 = \gamma_2 = 1$ (top), or asymmetric $\gamma_1 = 1 < \gamma_2 = \sqrt{3}$ (bottom). Contact tension $\gamma_c = 1$, pumping rate $\lambda_p = 0$.

Movie 9: simulation of coarsening in a regular hexagonal network of lumens.
Different tensions are imposed at ICM-ICM (blue, $\gamma_{TE} = 0.9$) and TE-ICM (red, $\gamma_{ICM} = 1$) interfaces. Contact tension $\gamma_c = 1$, pumping rate $\lambda_p = 0$.

Movie 10: simulation of the coarsening in a network of lumen representing a chimeric embryo with low contractility mutant cells.
Mutant TE cells (light green) have a lower contractility than WT TE cells (light magenta): lumen tensions are $\gamma_{mutant} = 0.7$ at the mutant/ICM interface (green), $\gamma_{TE\text{-}mutant} = [\gamma_{mutant} + \gamma_{TE}] / 2$ at the TE/mutant/ICM interface (grey), $\gamma_{TE} = 0.9$ at TE/ICM interface (magenta) and $\gamma_{ICM} = 1$ at the ICM interface (blue). Contact tension $\gamma_c = 1$, pumping rate $\lambda_p = 0$.

Authors contributions

HT and JLM conceptualized the project and acquired funding. JGD and JLM designed experiments. JGD, AFT and LDP performed experiments. JGD, AFT, LDP and JLM analysed the data. MLVS, AM and HT designed the theoretical model and performed the numerical simulations.

Methods

Embryo work

Recovery and culture

All animal work is performed in the animal facility at the Institut Curie, with permission by the institutional veterinarian overseeing the operation (APAFIS #11054-2017082914226001). The animal facilities are operated according to international animal welfare rules.

Embryos are isolated from superovulated female mice mated with male mice. Superovulation of female mice is induced by intraperitoneal injection of 5 international units (IU) pregnant mare's serum gonadotropin (PMSG, Ceva, Syncro-part), followed by intraperitoneal injection of 5 IU human chorionic gonadotropin (hCG, MSD Animal Health, Chorulon) 44-48 hours later. Embryos are recovered at E1.5 or E2.5 by flushing oviducts from plugged females with 37°C FHM (LifeGlobal, ZEHP-050 or Millipore, MR-122-D) using a modified syringe (Acufirm, 1400 LL 23).

Embryos are handled using an aspirator tube (Sigma, A5177-5EA) equipped with a glass pipette pulled from glass micropipettes (Blaubrand intraMark or Warner Instruments).

Embryos are placed in KSOM (LifeGlobal, ZEKS-050 or Millipore, MR-107-D) or FHM supplemented with 0.1 % BSA (Sigma, A3311) in 10 μL droplets covered in mineral oil (Sigma, M8410 or Acros Organics). Embryos are cultured in an incubator with a humidified atmosphere supplemented with 5% CO_2 at 37°C.

To remove the Zona Pellucida (ZP), embryos are incubated for 45-60 s in pronase (Sigma, P8811).

For imaging, embryos are placed in 5 or 10 cm glass-bottom dishes (MatTek).

Mouse lines

Mice are used from 5 weeks old on.

(C57BL/6xC3H) F1 hybrid strain is used for wild-type (WT).

To visualize plasma membranes, mTmG or mG (Gt(ROSA)26Sor[tm4(ACTB-tdTomato,-EGFP)Luo]) mice are used (*18*). To remove LoxP sites specifically in oocytes, Zp3-cre (Tg(Zp3-cre)93Knw) mice are used (*34*). To generate mCdh1 embryos, Cdh1[tm2kem] mice are used (*35*) to breed Cdh1[tm2kem/ tm2kem]; Zp3[Cre/+] mothers with mTmG or mG fathers. To generate mMyh9 embryos, Myh9[tm5RSad] mice are used (*36*) to breed Myh9[tm5RSad/tm5RSad]; Zp3[Cre/+] mothers with mTmG or mG fathers.

To visualize Cdh1, transgenic Cdh1-GFP mice were generated by the micro-injection of a bacterial artificial chromosome containing the Cdh1 gene modified by recombineering (RP23-262N14) (*20*, *37*) into (CD1xC57BL/6) F1 hybrid zygotes that were transferred into pseudo-pregnant CD1 female mice. Founder mice were examined for the presence of BAC integration

by genotyping using CACATGAAGCAGCACGACTT and AGTTCACCTTGATGCCGTTC primers amplifying 250bp of the BAC backbone and GACCACATGAAGCAGCACGAC and CGAACTCCAGCAGGACCATG primers amplifying 445bp of the GFP tag. Preimplantation embryos from positive mice were imaged to verify the junctional localization of the GFP signal in live embryos and in embryos stained using Cdh1 antibody. Mice were outcrossed to (C57BL/6xC3H) F1 hybrid mice to generate N1.

Chemical reagents

Blebbistatin (+), an inactive enantiomere of the inhibitor, or (-), the selective inhibitor myosin II ATPase activity, (Tocris, 1853 and 1852) 50 mM DMSO stocks are diluted to 25 μM in KSOM or FHM. 32-cell stage embryos are incubated in medium containing Blebbistatin without covering with mineral oil for 1 h before the beginning of the experiment.

KSOM containing 175 mM sucrose is made by diluting a 1.4 M sucrose KSOM preparation adapted from (*38*) into commercial KSOM. Late 16-cell stage and early 32-cell stage embryos are incubated and imaged overnight.

Y27632, a selective inhibitor of Rock (Tocris, 1254), 100 mM PBS stock is diluted to 10 μM in KSOM. Late 16-cell stage and early 32-cell stage embryos are incubated and imaged overnight.

Ouabain, a selective inhibitor of Na/K pump (Tocris, 1076), 100 mM DMSO stock is diluted to 1 mM in KSOM. Late 16-cell stage and early 32-cell stage embryos are incubated and imaged overnight.

Alexa Fluor 488 coupled to a 3 kDa Dextran (Sigma, D34682) is added to KSOM at 0.1 g.L^{-1}. Embryos are placed in labelled Dextran at the 16-cell stage before tight junctions fully seal.

Chimeric embryos

To build chimeras, 2- and 4-cell stage embryos are removed from their ZP using pronase and placed into Ca^{2+}-free KSOM for 2-3 min before being aspirated multiple times through a glass pipette until dissociation of cells into singlets or doublets. Using a mouth pipette, one 2-cell stage or two 4-cell stage blastomeres from two different embryos are then re-aggregated to form a complete embryo. We exclude chimeras in which fewer than half of the cells come from one of the two original embryos.

Immunostaining

Embryos are fixed in 2% PFA (Euromedex, 2000-C) for 10 min at 37°C, washed in PBS and permeabilized in 0.01% Triton X-100 (Euromedex, T8787) in PBS (PBT) at room temperature before being placed in blocking solution (PBT with 3% BSA) at 4°C for 4 h. Primary antibodies are applied in blocking solution at 4°C overnight. After washes in PBT at room temperature, embryos are incubated with secondary antibodies, DAPI and/or phalloidin at room temperature for 1 h. Embryos are washed in PBS and imaged immediately after.

Primary antibodies	Dilution	Provider
Atp1a	1:100	Santa Cruz Biotechnology, sc-21712
Aqp3	1:500	Novus Biologicals, NBP2-33872
Cdh1	1:500	eBioscience, 14-3249-82
Ctnnb1	1:100	Cell Signaling Technology, 8480
Pard6B	1:50	Santa Cruz Biotechnology, sc-166405
Prkcz	1:50	Santa Cruz Biotechnology, sc-17781

Secondary antibody and dyes	Dilution	Provider
Alexa Fluor Plus 488 anti-mouse	1:200	Invitrogen, A32723
Alexa Fluor 546 anti-mouse	1:200	Invitrogen, A11003
Alexa Fluor Plus 488 anti-rabbit	1:200	Invitrogen, A32731
Alexa Fluor 488 anti-rat	1:200	Invitrogen, A11006
Alexa Fluor 546 anti-rat	1:200	Invitrogen, A11081
Alexa Fluor 633 anti-rat	1:200	Invitrogen, A21094
Alexa Fluor 633 phalloidin	1:200	Invitrogen, A22284
DAPI	1:1000	Invitrogen, D1306

Micropipette aspiration

As described previously (*22, 23*), a microforged micropipette coupled to a microfluidic pump (Fluigent, MFCS EZ) is used to measure the surface tension of embryos. In brief, micropipettes of radii 25.5-31.5 μm are used to apply step-wise increasing pressures against the TE lining the blastocoel until reaching a deformation which has the radius of the micropipette (R_p). At steady-state, the surface tension γ of the blastocyst is calculated from the Young-Laplace's law applied between the embryo and the micropipette: $\gamma = P_c / 2 \, (1/R_p - 1/R)$, where P_c is the critical pressure used to deform the embryo of radius R. Based on this measurement, we then use the Young-Laplace law between the blastocyst and the outside medium to calculate the hydrostatic pressure P of the embryo: $P = 2 \, \gamma / R$.

Microscopy

Live imaging is performed using an inverted Zeiss Observer Z1 microscope with a CSU-X1 spinning disc unit (Yokogawa). Excitation is achieved using 488 and 561 nm laser lines through a 63x/1.2 C Apo Korr water immersion objective. Emission is collected through 525/50 and 595/50 band pass filters onto an ORCA-Flash 4.0 camera (C11440, Hamamatsu). The microscope is equipped with an incubation chamber to keep the sample at 37°C and supply the atmosphere with 5% CO_2.

Surface tension measurements are performed on the same microscope using a 40x/0.95 Plan Apo Korr dry objective without CO2 supply in FHM medium.

Immunostainings are imaged on the same microscope using 405, 488, 561 and 642 nm laser lines through a 63x/1.2 C Apo Korr water immersion objective, 450/50 nm, 525/50 nm, 595/50 band pass or 610 nm low pass filters. Alternatively, an inverted Nikon Eclipse-Ti microscope with a CSU-X1 spinning disc unit (Yokogawa) is used. Excitation is achieved using 405, 488, 561 and 642 nm laser lines through a 60x/1.4 oil immersion DIC N2 PL APO VC objective. Emission is collected through 525/50 nm, 605/40 nm, 629/62 nm band pass or 640 nm low pass filters onto a CoolSnap HQ2 camera. Otherwise, a scanning confocal Zeiss LSM700 equipped with 405, 488, 555 and 639 nm laser lines is used. Acquisition through a 63x/1.4 OIL DICII PL APO objective onto PMTs.

High temporal resolution imaging is performed using a Viventis Microscopy LS1 Live light-sheet microscope. Fluorescence excitation was achieved with a dual illumination scanned Gaussian beam light sheet of ~1.1 μm full width at half maximum using 488 and 561 nm lasers. Signal was collected with a Nikon CFI75 Apo LWD 25x/1.1 objective and through 525/50-25 or 561/25 band pass filter onto an Andor Zyla 4.2 Plus sCMOS camera. The microscope is equipped with an incubation chamber to keep the sample at 37°C and supply the atmosphere with 5% CO_2.

Data analysis

Microlumens area

Using FIJI (*39*), we track a given cell-cell contact over time and measure all of its microlumens by identifying their equatorial plane in 3D. We draw the outline of all individual microlumens and measure in 2D their cross-sectional area over time. Using R, we fit the dynamics of microlumens area with a piece-wise linear regression considering a single inversion point (*40, 41*). This delivers two slopes giving the swelling and discharge rates as well as the inversion times for a given contact.

Cells are determined to be TE or ICM based on the presence or absence of contact to the outside medium respectively. Interfaces are classified as a "near" or "away" from the final position of the blastocoel by locating the blastocoel and bisecting the embryo in two halves, one with and the other without the blastocoel in it.

Radius of curvature

Using FIJI, we select a cell interface that is in the equatorial plane of two contacting cells. We manually fit a circle onto the interface or onto either sides of the microlumen. For the curvature

of cell-cell interfaces, we measure all interfaces that can be measured in fixed embryos with (+) or (-) Blebbistatin. For microlumen measurements, we measure all microlumens that are large enough to be measured 60 min after the time of inversion.

Cells are determined to be TE or ICM based on the presence or absence of contact to the outside medium respectively. Interfaces are classified as a "near" or "away" from the final position of the blastocoel by locating the blastocoel and bisecting the embryo in two halves, one with and the other without the blastocoel in it. Images and ROIs are provided.

Blastocoel location in chimeric embryos

Cells from chimeric embryos are classified as ICM when they have no contact to the outside medium, as mural TE when they have a contact with the outside medium and with the blastocoel and as polar TE when they have a contact with the outside medium and no contact with the blastocoel.

The number of cells from either donor embryo is counted for each tissue (ICM, polar and mural TEs). We calculate the relative proportion of each donor embryo to each tissue and the ratio of mural TE to the total TE for a given donor embryo. Images and ROIs are provided.

Apical/basal intensity ratio

Using FIJI, we select confocal slices cutting through the equatorial plane of a TE cell lining the blastocoel. We draw a ~1 μm thick segmented line along the cell-medium interface and measure the mean apical intensity. We draw a line spanning the cell-cell contacts and blastocoel interface and measure the mean basal intensity. We then calculate the apical to basal ratio. We measured 3 cells per embryo. Images and ROIs are provided.

Variability ratio

Using FIJI, we select confocal slices cutting through the equatorial plane of a cell. We measure 90 min before the appearance of the first microlumens and 90 min after. Using a 1 μm thick segmented line, we draw along the cell-cell contact and we measure the mean and standard deviation of the intensity along this contact. The coefficient of variation is calculated by dividing the standard deviation by the mean intensity. The variability ratio is determined by dividing the coefficient of variation before and after the appearance of microlumens.

For embryos that do not form a blastocoel (when treated with Ouabain, Y27632 or sucrose), the latest time of appearance of microlumens is determined in control embryos from the same experiment. Measurements are then performed 90 min before and 90 min after this time. Images and ROIs are provided.

Cells are determined to be TE or ICM based on the presence or absence of contact to the outside medium respectively. Interfaces are classified as a "near" or "away" from the final position of the blastocoel by locating the blastocoel and bisecting the embryo in two halves.

Cell and blastocoel volume measurement

28

Using LimeSeg (*31*) on 1 *µ*m-spaced confocal slices of mTmG embryos, we computationally segment the volume of cells and of the blastocoel. We track cell volumes every 5 min from 25 min before the appearance of microlumens to 120 min after (corresponding to the phase of initial expansion of the blastocoel).

Statistics

Mean, standard deviation, minimum, maximum, lower and upper quartiles, median, paired and two-tailed Student's *t*-test, single-tailed Mann-Whitney *U*-test and Chi-squared *p* values are calculated using Excel (Microsoft) or R (R Foundation for Statistical Computing). Statistical significance is considered when $p < 10^{-2}$. Whisker plots show the minima, lower quartiles, medians, upper quartiles and maxima.

The sample size was not predetermined and simply results from the repetition of experiments. No sample was excluded. No randomization method was used. The investigators were not blinded during experiments.

Code and data availability

The microscopy data, ROI and analyses are available on the following repository under a CC BY-NC-SA license: https://ressources.curie.fr/frackening

The code of the simulations is available on the following repository under a MIT license: https://github.com/VirtualEmbryo/lumen_network

Supplementary Text

In this Supplementary Text section, we introduce the main hypotheses and equations of the physical model and the methods underlying the numerical simulations.

Main hypotheses of the model

The physical model approximates the problem in 2 dimensions and aims at calculating the hydraulic fluxes between lumens within the embryo to characterize their coarsening.

Hydrostatic pressure gradients between lumens

A gradient of hydrostatic pressure must exist to generate a flux between two lumens. The intercellular space width lies in the range $d \sim 20 - 100\,\mathrm{nm}$ (42). It is supposed small compared to distance L between microlumens, of the order of a few $100\,\mathrm{nm}$ to μms, and we describe the flow in the intercellular space in the lubrication's limit ($d \ll L$). The flow rate Q between two positions is therefore given by the Hagen-Poiseuille's formula

$$Q = -\kappa_v \Delta P \tag{1}$$

with ΔP the pressure difference between lumens and $\kappa_v = \frac{d^3}{12\eta}$ an effective friction coefficient, which depends on the intercellular width d and on water viscosity $\eta \sim 10^{-3}\,\mathrm{Pa.s}$. We note that this formula is valid both for a thin film (as in the embryo) and for a 2D channel (as in our 2D model).

Mechanical interplay between cells and lumens

The lumens are confined between cells, which are exerting a cellular pressure on them. The hydrostatic pressure in a lumen may be related via Laplace's law to a tension γ and to a curvature radius R as $P - P_{\mathrm{ref}} = 2\gamma/R$. To predict the luminal flux direction between two lumens, their pressures have therefore to be compared relative to a common reference value P_{ref}, which may be advantageously chosen as a cell pressure. In Fig. S10 we inferred, through interface curvature measurement, the pressure difference between ICM-ICM, TE-ICM and TE-TE cell pairs. This reveals a higher pressure in ICM cells, which bulge into their TE counterparts. On the contrary, the relatively flat interfaces between cells of the same type hint towards similar cell pressures.

In our model, we neglect the direct mechanical interplay between cells and lumens, by collecting both cells pressure and higher surface contractility effects into a single lumen tension. Accordingly, we do not consider asymmetric lumens in order to reduce the number of parameters (see Supplementary Text Fig. 2), but the model could be easily generalized to asymmetric shapes, without loss of generality. These simplifying approximations are justified in details below

- At homotypic interfaces (ICM-ICM or TE-TE) we expect symmetric lumen shapes and the same reference pressure, making our approximations fully valid. [1]

---

[1] Note that we do not consider the lumens at TE-TE interfaces in the model, because the blastocoel expands and fills the entire TE-TE intercellular space, which ends up indistinguishable from the TE-ICM intercellular space. A large lumen growing from a TE-TE interface would lead to the same situation, so effectively we only need to resolve the competition between lumens at ICM-ICM and TE-ICM interfaces.

- At heterotypic interfaces, the lumen shape is found asymmetric, bulging more into TE than into ICM cells. This is expected from a higher lumen tension at the ICM interface and a higher ICM cell pressure, both resulting from of a higher contractility in ICM cells. The higher pressure in ICM cells is also partly due to their lower volume (Fig. S10). We chose to combine both effects, which add up, into a single lumen tension only.

The tensions we consider in the model should therefore be viewed as an average of the tensions at the two lumen interfaces: $\gamma_{\text{ICM-ICM}} = (\gamma_{\text{ICM}} + \gamma_{\text{ICM}})/2$, for ICM-ICM contacts, and $\gamma_{\text{TE-ICM}} = (\gamma_{\text{ICM}} + \gamma_{\text{TE}})/2$, for TE-ICM contacts, corresponding to a mean tension. In the following, we will denote them simply respectively as γ_{ICM} and γ_{TE} to simplify the notation.
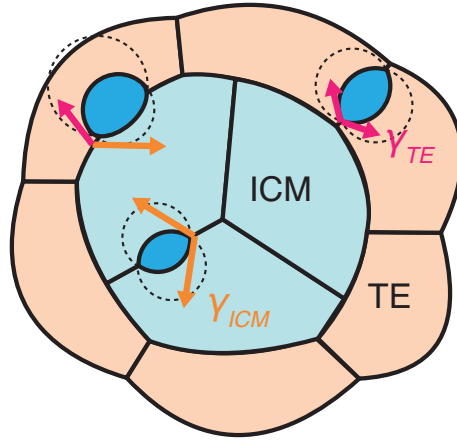
Supplementary Text Figure 1: Schematics of an embryo with ICM and TE cells with lumens at three different types of cell contacts. Curvatures are represented by dotted circles.

Lumen formation and fluid pumping

The model does not intend to model the formation of lumens, which may involve more intricate molecular details (membrane and adhesion dynamics, osmotic balance and possibly exocytosis). Instead, we start from a preformed network of microlumens and focus on the subsequent coarsening mechanism. To obtain statistically relevant averages, we average the simulation results over a large number of initial lumen areas, taken randomly from a given distribution (see section *Area dynamics in a lumen network*).

The model also ignores the details of the osmotic balance between the lumens and the cells, which would require further experimental characterization. Instead, we assume a constant and uniform pumping rate λ_p within the network, defined per unit length (in 2D). This hypothesis is equivalent to say that the density of pumps at baso-lateral interfaces within the embryo remains uniform in space and time. The area growth rate of a lumen will therefore increase with the size of its interfaces. For vanishing λ_p, the total area in the network will be conserved. We show in section *Variation of the pumping rate* that the positioning of the final lumen by coarsening is relatively independent of pumping, in particular the biphasic dynamics, which characterizes the coarsening process.

Area dynamics for two lumens

We consider first the case of two connected lumens in 2D. Each lumen i is characterized by its curvature radius R_i, tension γ_i and pressure P_i. Force balance takes the form of Laplace's law

$$P_i = \frac{\gamma_i}{R_i} \tag{2}$$

and tension balance at edge of the lumen

$$2\gamma_i \cos(\theta) = \gamma_{ci} \tag{3}$$

where γ_{ci} is the tension at the cell-cell contact for the lumen i.

Laplace's pressure in one lumen

The pressure inside each lumen i is calculated as function of its area from geometrical considerations, using the contact angle θ_i (see Supplementary Text Fig. 2). The area A_i of the lumen i can be decomposed as

$$A_i = A_{\text{channel}} + 2A_{1/2} = 2R_i d \sin(\theta_i) + R_i^2 \left[2\theta_i - \sin(2\theta_i) \right]$$
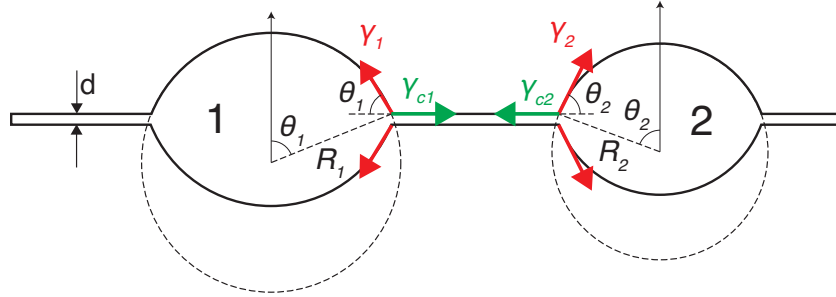
Supplementary Text Figure 2: Geometrical parametrization of two lumens exhanching fluid via a channel of diameter d. Each lumen is symmetric, with radius of curvature R_i and contact angle θ_i ($i = 1, 2$). The lumen tensions γ_i and contact tensions $\gamma_{c,i}$ depicted are satifying tension balance in Eq. (3).

Assuming $d \ll R_i$ we find

$$A_i \simeq R_i^2 \left[2\theta_i - \sin(2\theta_i) \right] \tag{4}$$

and it yields

$$R_i \simeq \sqrt{\frac{A_i}{2\theta_i - \sin(2\theta_i)}} \tag{5}$$

hence, using Eq. (2), we find the pressure of the lumen to be

$$P_i = \frac{\gamma_i \Gamma_i}{\sqrt{A_i}} \tag{6}$$

where $\Gamma_i \equiv \sqrt{2\theta_i - \sin(2\theta_i)}$.

Hydraulic flux and phase diagram

Two lumens with different curvatures and/or tensions will have different Laplace's pressures, which gives rise to a pressure gradient and hence to a flow of fluid from the lumen with higher pressure to the one with a lower pressure. If we denote the two lumens 1 and 2, and assuming mass conservation $A_{\text{tot}} = A_1 + A_2 = \text{cte}$, the time evolution for the size of the lumens is given by the dynamical equation

$$\frac{dA_1}{dt} = -\frac{dA_2}{dt} = I_{1,2} \equiv \frac{P_2 - P_1}{\mathscr{R}_{12}} \tag{7}$$

where we denoted $I_{1,2}$ the flux from lumen 2 to 1 ($I_{2,1} = -I_{2,1}$ from 1 and 2). $\mathscr{R}_{12}$ is the hydraulic resistance of the channel, which is proportional to its length ℓ_{12}

$$\mathscr{R}_{12} = \frac{\ell_{12}}{\kappa_v} \tag{8}$$

κ_v is a friction coefficient given by Poiseuille's law, that depends on the channel width d and fluid viscosity η. For a 2-dimensional channel, its expression is given by $\kappa_v = \frac{d^3}{12\eta}$.

Eq. (7) is a deterministic equation, and for given initial conditions, we can predict which lumen between 1 and 2 will win, i.e. will grow, knowing the sign of the flux I_{12}. The pressures P_i are given by Eq. (6). Thus, if $P_2 > P_1$, the lumen 1 grows. Expressing the flux I_{12} as function of the parameters γ_i, γ_{ci} and A_i for $i = 1, 2$, we can build a phase diagram for the direction of the flux is summarized in Supplementary Text Fig. 3.
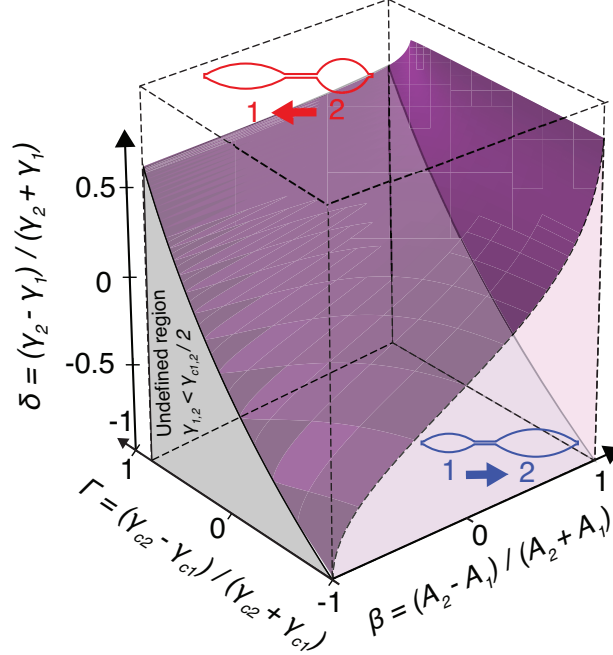
Supplementary Text Figure 3: Phase diagram for the direction of the fluid flux between two lumens as function on the area asymmetry $\beta = \frac{A_2 - A_1}{A_2 + A_1}$, lumen tension asymmetry $\delta = \frac{\gamma_2 - \gamma_1}{\gamma_2 + \gamma_1}$ and adhesive contact tension asymmetry $\Gamma = \frac{\gamma_{c2} - \gamma_{c1}}{\gamma_{c2} + \gamma_{c1}}$. The volume below the purple surface correspond to parameters such that the fluid flux goes from lumen 1 to lumen 2.

24

Pumping

We now consider the case where the lumen is able to pump additional fluid through its interface. The flux $I_p(\theta_i, A_i)$ of pumped fluid is assumed to be proportional to the lumen contour

$$\mathscr{L}_i = 2 \times 2\theta_i \sqrt{\frac{A_i}{2\theta_i - \sin(2\theta_i)}}$$

and is characterized by a constant pumping rate per unit length λ_p. Here, we do not consider pumping in the channel itself. For an isolated lumen i with pumping, the time evolution of its size is given by

$$\frac{dA_i}{dt} = I_p(\theta_i, A_i) = \lambda_p \mathscr{L}_i = 4\lambda_p \theta_i \sqrt{\frac{A_i}{2\theta_i - \sin(2\theta_i)}} \tag{9}$$

For the case of two connected lumens with the same pumping rate λ_p, their time evolution is now given by the equations

$$\begin{cases} \frac{dA_1}{dt} &= I_{1,2} + I_p(\theta_1, A_1) \\ \frac{dA_2}{dt} &= I_{2,1} + I_p(\theta_2, A_2) \end{cases} \tag{10}$$

Area dynamics in a lumen network

Dynamical equations

We can easily generalize Eq. (10) for a network of n lumens $i = 1, \ldots, n$. The network is described as an undirected graph $G = \{V, E\}$, where V is a set of vertices representing the lumens $i = 1, \ldots, n$. and E is a set of edges $(i, j) \in V \times V$ representing the channels. The dynamics are described by a set of coupled ordinary equations for $i = 1, \ldots, n$.

$$\frac{dA_i}{dt} = \sum_{j \in \partial_i} I_{i,j} + I_p(\theta_i, A_i) \tag{11}$$

with ∂_i is the set of neighbors of the lumen i. Therefore, each lumen is described by one variable, its area A_i and characterized by two parameters: its tension γ_i, the contact tension γ_{ci}. The pumping rate λ_p is a global parameter for the whole network.

Numerical simulations

The numerical simulations have been implemented in *Python* and the code is available on GitHub https://github.com/VirtualEmbryo/lumen_network.

Graph generation   We generate the lumen network as a set of connected vertices. Each vertex is a lumen with coordinates (x, y), connected to its neighbors. Self-loops are not allowed. The coordinates of the points are saved in a file (*lumen_coord.dat*) for graphic representation. The topology of the network can be chosen arbitrarily, but it is restricted here to hexagonal or triangular lattices. To each point is associated an initial area A, drawn from a truncated normal distribution $N(\mu, \sigma)_{A>p}$, such that $p = 0.1$. The parameters of the normal distribution are chosen as $\mu = 1$

and $\sigma = 0.1$ here. We verified that our results do not change qualitatively with this particular choice. To each lumen i is associated a lumen tension γ_i and a contact tension $\gamma_{c,i}$, that set the lumen contact angle θ_i (Eq. (3)). The structure of the graph (set of edges) is saved in a file (*lumen_lumen.dat*), with the length of each edge ℓ_{ij}, determining its hydraulic resistance $\mathscr{R}_{12}$ (Eq. (8)). The initial parameters of the lumen (set of vertices) are saved in another file (*lumen.dat*) to allow averaging over the same structures. Other files are needed for the algorithm to process, such as a configuration file (*test.ini*) that sums up the input parameters, such as the channel width (we chose here $d = 0.01$). We call *regular* a lattice where vertices are equidistant from each others (usually, the length is set to 1), imposing hence the same resistance for every edge (i,j).

Bridges   When the network is evolving, some lumens will shrink and their area will tend to zero. To avoid divergence, we consider that a lumen i as empty when $A_i < d^2$. An empty lumen cannot grow anymore but can still let the fluid pass through. If the empty lumen connects two lumens only, it is deleted from the network, and the distance between the neighbors is calculated summing the two initial channel lengths (e.g. if lumen 2 connects 1 and 3 but disappears, $\ell'_{13} = \ell_{12} + \ell_{23}$). If the empty lumen has only one neighbor, it simply disappears from the graph. If the disappearing lumen is connected to more than two lumens, it will be replaced by a *bridge*. A bridge has an area A_b equal to zero and simply let fluid pass through. Its pressure P_b is calculated from mass conservation, stating that the incoming fluxes on a bridge should sum to zero (Kirchhoff's law):

$$
\begin{aligned}
0 &= \sum_{j \in L_b} \frac{P_j - P_b}{\mathscr{R}_{bj}} + \sum_{j \in B_b} \frac{P_j - P_b}{\mathscr{R}_{bj}} \\
&= \sum_{j \in L_b} \frac{P_j}{\mathscr{R}_{bj}} + \sum_{j \in B_b} \frac{P_j}{\mathscr{R}_{bj}} - P_b \sum_{j \in L_b \cup B_b} \frac{1}{\mathscr{R}_{bj}} \\
&= C_b + R_{j,b} P_j + R_{b,b} P_b
\end{aligned}
$$

where L_b and B_b designate the set of neighboring lumens and bridges connected to a bridge b. Considering all bridge pressures, collected within a vector $\vec{P}$, the coupled equations above yield a linear system

$$
\underline{\underline{R}}.\vec{P} = \vec{C} \tag{12}
$$

The vector $\vec{C}$ collects the pressures of the lumens weighted by the hydraulic resistances of channels linking bridges with their neighboring lumens, and the matrix $\underline{R}$ is a matrix with coefficients $r_{i,j} \equiv 1/\mathscr{R}_{ij}$ for $i \neq j$ and $r_{i,i} = -\sum_{j \in L_i} r_{i,j}$.

The two types of connections to a bridge, i.e. *bridge-lumen* and *bridge-bridge*, are stored in specific data files (*bridge_lumen.dat* and *bridge_bridge.dat* respectively). As the network evolves, the number of lumens will decrease, reducing the computational cost of the simulation for large networks.

Numerical scheme   The numerical integration of the set of equations Eq. (11) is done using the library **scipy.integrate** from Python2.7, more precisely the method *odeint*[2]. Since the method does not provide an event handle to detect if a lumen is empty, the numerical solving is done by restarting the integration for small time frames, checking the conditions and starting it again.

---

[2]See documentation: https://docs.scipy.org/doc/scipy/reference/generated/scipy.integrate.odeint.html
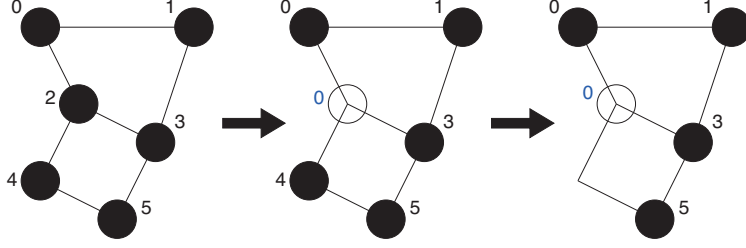
Supplementary Text Figure 4: A simple network evolution. Lumen 2 becomes bridge 0, then lumen 4 disappears but the link between bridge 0 and lumen 5 still exists.

However, because of the dynamics, the disappearance of lumens will change the network quickly at small times, and more slowly at larger times. Moreover, the dynamics at large times is much slower than at small times, because of the competition between larger lumens is slower. We therefore implemented an *adaptive time stepping*, that depends on the number of lumens N as

$$t_{\text{step}} = \frac{a}{N^2} \tag{13}$$

where $a = 0.1$ is an arbitrary constant, chosen to obtain a smooth dynamics. The time frame for which the integration proceeds before conditions are checked again is set as $t_{\text{frame}} = k.t_{\text{step}}$, with $k = 20$ an arbitrary constant.

The calculation of the area change $\frac{dA_i}{dt}$ is split into four steps :

1. the flux through between lumens i and $j \in \partial_i$, $I_{ij} = \frac{P_j - P_i}{\mathscr{R}_{i,j}}$ is calculated, adding I_{ij} to $\frac{dA_i}{dt}$, subtracting $I_{ji} = -I_{ij}$ to $\frac{dA_i}{dt}$.

2. the bridge pressures are calculated by solving the linear system (12) using the library **numpy.linalg**, with the method **solve**.

3. similar to 1., the fluxes through bridge-lumen connections are calculated, $I_{ib} = \frac{P_b - P_i}{\mathscr{R}_{i,b}}$.

4. if pumping is included and the lumen is not empty, then the area change for lumen i is calculated using Eq. (9).

In the end, the area change for lumen i is given by

$$\frac{dA_i}{dt} = \sum_{j \in L_i} I_{ij} + \sum_{b \in B_i} I_{ib} + I_p(\theta_i, A_i) \tag{14}$$

The simulation is terminated when only one non-empty lumen remains. Areas are stored in an output file (*area.dat*), and each time step is recorded. The area conservation is checked at every step, and errors are stored in a log file (*error.log*). The initial and final configurations are stored in a third file (*area.log*) in order to give an easy access to the important observables. A fourth file tracks the disappearance and relabeling of lumens into bridges if needed, as well as the reconnections in the graph.
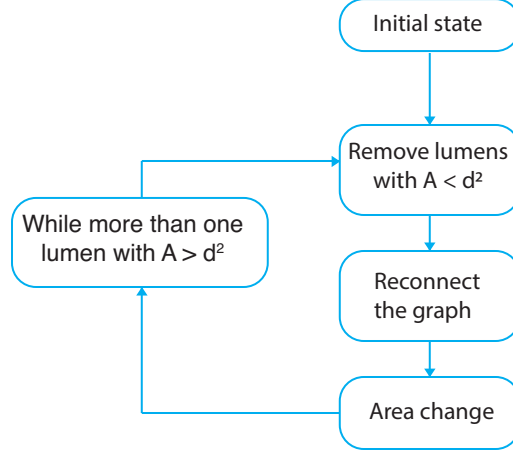
Supplementary Text Figure 5: Basic steps of the script.

Robustness of the simulations

In this section, we present additional results to show the robustness of our simulations. We will denote $\delta_{\text{TE-ICM}} = (\gamma_{\text{TE}} - \gamma_{\text{ICM}})/(\gamma_{\text{TE}} + \gamma_{\text{ICM}})$ the tension asymmetry where γ_{TE} and γ_{ICM} are the tensions of a lumen respectively at the TE-ICM interface or ICM-ICM interface.

Variation of the initial area distribution

The initial area distribution of the lumens is a truncated Gaussian distribution

$$A \hookrightarrow \mathcal{N}(\mu, \sigma)_{A>p} \tag{15}$$

such that $\mu = 1$. $p = 0.1$ is an arbitrary constant and minimal initial area allowed. The width of the distribution is usually taken to be $\sigma = 0.1$. Supplementary Text Fig. 6 shows the effect of broader distributions on the probability for the final lumen to be at the TE-ICM interface: as the width of the area distribution increases, the sharpness of the transition decreases. This can be simply interpreted as the consequence of an increased probability of starting with a large initial lumen in a region of larger tension, the size asymmetry compensating the imposed tension asymmetry.
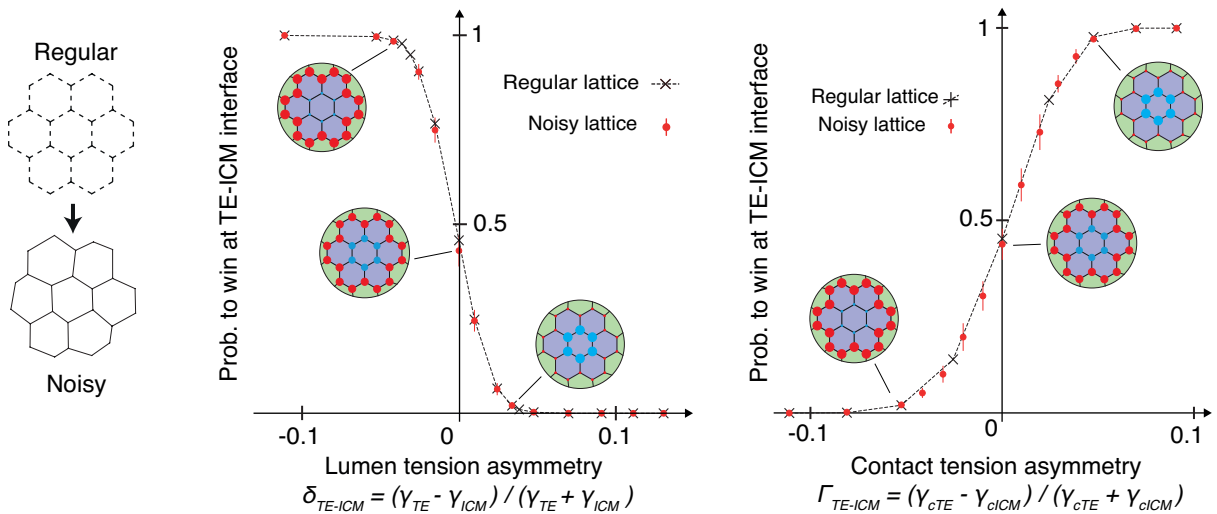
Irregular lattices

Networks are generated from regular lattices, with identical distances between lumens. *Noisy* lattices are generated from a regular lattice, by displacing randomly the positions of the vertices by a vector $d\vec{u} = (dx, dy)$ of components $d\vec{u}$ drawn from a normal distribution $\mathcal{N}(0, 0.05)$. For a given lumen network, multiple configurations are averaged with the same number of simulations each. Noisy lattices show no deviations from the winning probability distribution of regular lattice, for both the tension asymmetry coefficient δ and contact tension asymmetry coefficient Γ (see Supplementary Text Fig. 7).

Variation of the network topology

We also tested two different topologies: hexagonal and triangular lattices. Hexagonal lattices are preferred as they more faithfully represent the connection between cells in 2 dimensions, corre-
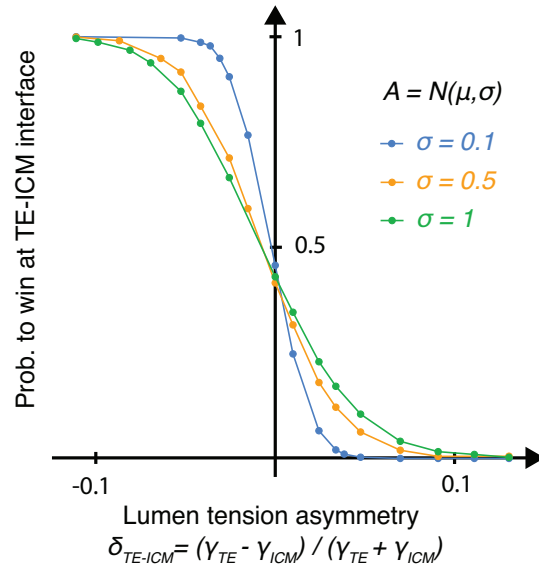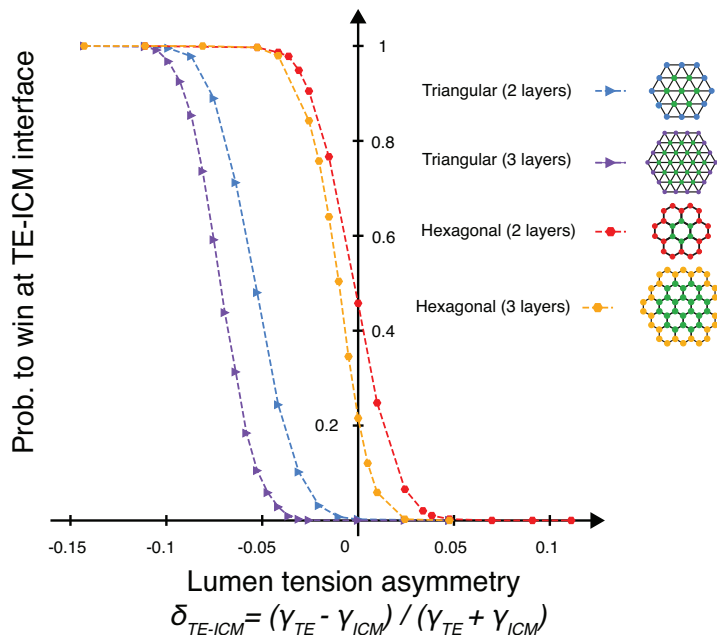
Supplementary Text Figure 6: Winning probability for lumens at the TE-ICM interface (external layer) for a regular hexagonal lattice with 2 layers, for different widths of the initial areas distribution. The initial areas are drawn from a truncated normal law ($A > 0.1$) with the same average ($\mu = 1$) but different standard deviations ($\sigma = 0.1, 0.5, 1$). The lumen network is the regular network similar to the one used in Fig. 3C. Each point results from at least 5000 simulations.

Supplementary Text Figure 7 (Left) A hexagonal noisy lattice (bottom), calculated from the regular hexagonal (top) lattice. (Center and right) Winning probability for lumens at the TE-ICM interface (external layer) for regular (red crosses, dashed lines) and noisy (red dots, red vertical bar for standard deviation) hexagonal lattices, as functions of the tension asymmetry δ (center) and the contact tension asymmetry (right). Each point of the regular lattice results from at least 2000 simulations, the noisy lattice is the average of 25 configurations of the noisy lattice, 2000 simulations each.

sponding essentially to tricellular junctions. Triangular lattices are on the contrary more akin to an isotropic network. The TE-ICM interface is defined as the outer layer, with $\gamma_{ICM} = 1$ and γ_{TE} changed to tune the tension asymmetry δ. The topology or size of the network do not affect the qualitative behavior of the curve. However, an isotropic topology favors generally lumens inside the network and increasing the size of the network also marginally displaces the curve towards lower δ (see Supplementary Text Fig. 8). Hence as the network grows in size, we expect a higher asymmetry to be necessary to statistically direct the final lumen towards the network boundary.

Supplementary Text Figure 8: Winning probability for lumens at the TE-ICM interface (external layer) for regular hexagonal and regular triangular lattices of different sizes. An inset shows the lattices with lumens (green for ICM-ICM, colored for TE-ICM). Each point results from at least 2000 simulations.

Variation of the pumping rate

We studied whether including pumping affects the coarsening process (see Eq. (11)).

For small pumping rates ($\lambda_p \lesssim 1.10^{-3}$ with all tensions at 1), the coarsening dynamics is slightly modified, but the precise order of lumen disappearance does not change significantly (Supplementary Text Fig. 9).

However, above a certain value of pumping (here $\lambda_p \gtrsim 4.10^{-3}$), the system is unable to coarsen into a one final lumen: two lumens will keep growing faster than their rate of fluid exchange (see Supplementary Text Fig. 9).

Adding pumping also makes the probability curve to win at the TE-ICM interface as function of the tension asymmetry more abrupt, but does not change qualitatively its shape (see Supplementary Text Fig. 10). However, no obvious effect is observed for variations of the contact tension asymmetry Γ.
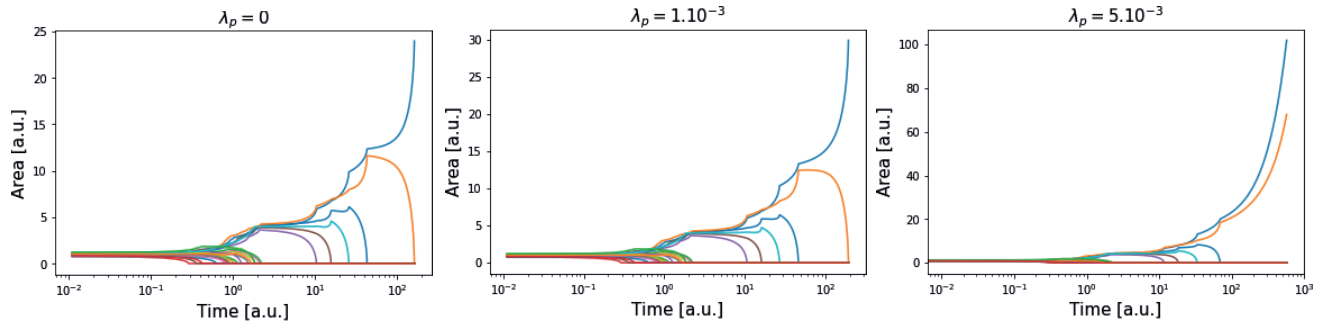
Supplementary Text Figure 9. Network coarsening dynamics of a hexagonal network (2 layers), for different pumping rates: no pumping ($\lambda_p = 0$), and $\lambda_p = 1.10^{-3}$, 5.10^{-3}.
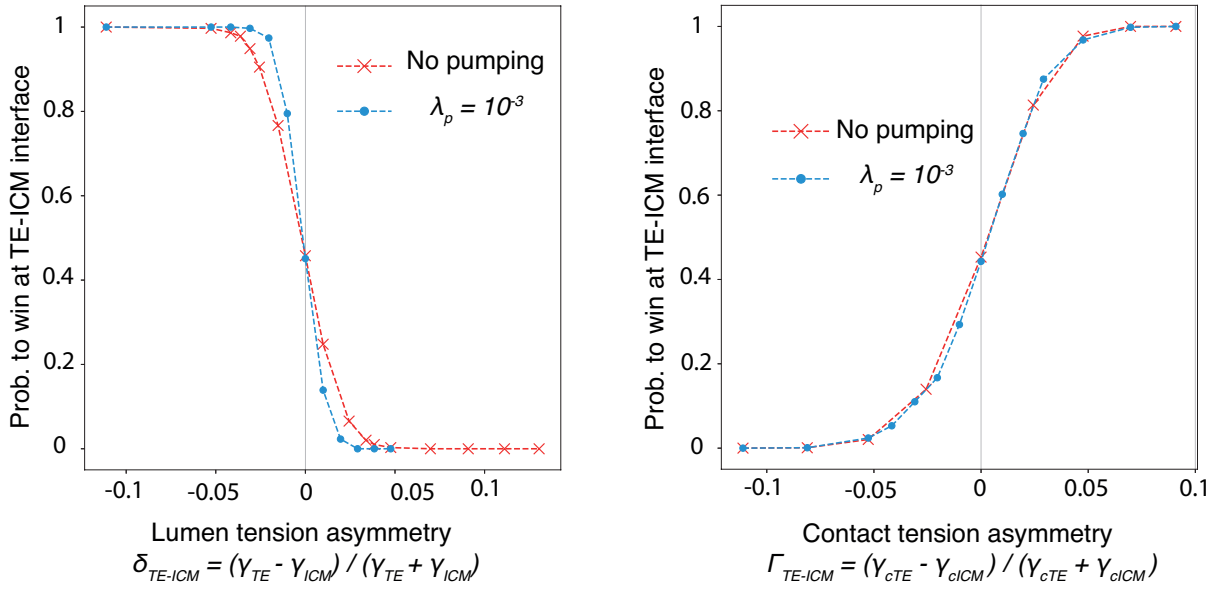
Supplementary Text Figure 10. Winning probability for lumens at the TE-ICM interface (external layer) with (blue dots) and without (red crosses) pumping. The pumping rate λ_p is chosen so that the dynamics of the coarsening does not blow up. Each point corresponds to the average of at least 1000 simulations.